5-2022

Non-Contact Vital Sign Detection Using mm-Wave Radar

Marvin Joshi
University of Tennessee, Knoxville, mjoshi5@vols.utk.edu

Recommended Citation

Joshi, Marvin, "Non-Contact Vital Sign Detection Using mm-Wave Radar. " Master's Thesis, University of Tennessee, 2022.
https://trace.tennessee.edu/utk_gradthes/6384

To the Graduate Council:

I am submitting herewith a thesis written by Marvin Joshi entitled "Non-Contact Vital Sign Detection Using mm-Wave Radar." I have examined the final electronic copy of this thesis for form and content and recommend that it be accepted in partial fulfillment of the requirements for the degree of Master of Science, with a major in Electrical Engineering.

Aly E. Fathy, Major Professor

We have read this thesis and recommend its acceptance:

Benjamin J. Blalock, David Icove

Accepted for the Council:
Dixie L. Thompson

Vice Provost and Dean of the Graduate School

(Original signatures are on file with official student records.)

To the Graduate Council:
I am submitting herewith a thesis written by Marvin Joshi entitled "Non-Contact Vital Sign Detection Using mm-Wave Radar." I have examined the final paper copy of this thesis for form and content and recommend that it be accepted in partial fulfillment of the requirements for the degree of Master of Science, with a major in Electrical Engineering.

Aly E. Fathy, Major Professor

We have read this thesis
and recommend its acceptance:

Benjamin J. Blalock

David Icove

Accepted for the Council:

Dixie L. Thompson

Vice Provost and Dean of the Graduate School

To the Graduate Council:
I am submitting herewith a thesis written by Marvin Joshi entitled "Non-Contact Vital Sign Detection Using mm-Wave Radar." I have examined the final electronic copy of this thesis for form and content and recommend that it be accepted in partial fulfillment of the requirements for the degree of Master of Science, with a major in Electrical Engineering.

Aly E. Fathy, Major Professor

We have read this thesis
and recommend its acceptance:

Benjamin J. Blalock

David Icove

Accepted for the Council:

Dixie L. Thompson

Vice Provost and Dean of the Graduate School

(Original signatures are on file with official student records.)

Non-Contact Vital Sign Detection Using mm-Wave Radar

A Thesis Presented for
Master of Science
Degree
The University of Tennessee, Knoxville

Marvin Joshi
May 2022

To my family and friends.

Acknowledgements

I would like to first start off with thanking Dr. Aly Fathy for letting me join his lab and for all his expertise. From taking his classes to being in his research group, he has helped me learn and grow in so many ways. To Dr. Blalock and Dr. Icove, thank you for being apart of my committee and for making your courses an enjoyable place to learn.

I would like to thank everyone in Dr. Fathy's research group: Chandler Bauder, Abdel Kareem Moadi, Peter Alley, Toan Vo Dai and Tsotne Kvelashvili. To Chandler and Abdel, thank you helping me when I was first learning about vital sign detection and incorporating me in their work. A special thanks to Abdel, Chandler and Peter for assisting me with all my measurements and making the lab an enjoyable place to work. The last two years wouldn't be as fun as it was without them.

Thank you to my father, Pooran Joshi, my mother, Mamta Joshi, and my sister, Shivani Joshi, for all of their support and love. Without them, I would not be where I am today. To Buddy, Sally, and Bob, thank you for making everyday enjoyable.

Abstract

Vital Sign detection using radars has been a rising technology in the fields of healthcare, security, and military purposes. Typically, radars used for these tasks operate at lower frequencies due to their low cost and and the ability to detect behind obstacles, such as walls or undre debris. However, this leads to an overall large system as the lower the frequency of operation, the larger the size of the antennas. The system size increases when multiple antennas are used for subject localization. But, with the development of millimeter-wave radars and Antenna-on-Package (AoP) solutions, a more compact and portable radar is possible. In this thesis, a commercial, compact, and portable millimeter wave radar operating at 60 GHz is used to detect the vital signs of subjects. With the use of direction of arrival, beamforming, and frequency tracking, the millimeter wave radar is able to accurately detect the heart rate and respiration rate of subjects with high accuracy. Experiments are performed involving detection with varying distances, detection through drywall, and for a single or even multiple subjects.

Table of Contents

List of Tables

List of Figures

Chapter 1

Introduction

In this chapter, a background of vital detection will be given followed by the motivation of using a millimeter wave radar for this work. Next, the state of the art work in this field is discussed followed by the scope, objectives and contributions of this work.

The ability to detect a human vitals signs, such as heart rate and respiration rate, provide important information for monitoring human health. Traditionally, contact sensors, such as pulse oximeters or chest belts are attached onto the human body. These sensors can be seen in Figure 1.1. While popularly used, these sensors are required to be in contact with the human's skin. Due to this, there are cases in which it is not possible to use these sensors. For example, in scenarios involving patients with burn injuries, the use of contact sensors is not possible. This same problem exists for babies that are born premature, as their skin is much more sensitive.

For these scenarios, non contact techniques are needed. Non contact solutions have been developed using camera-based photoplethysmography (PPG) or radar techniques. While both solutions offer high accuracy, radars can be used for more applications as they allow for non line of sight measurements, such as through walls, wood, or poor lighting conditions. See through walls allows for vital sign detection to be performed in scenarios involving disaster

Figure 1.1: Examples of Heart and Respiration Rate Contact Sensors

relief or for military applications. For instance, a radar would allow first responders to detect people, from their heart rate, that are underneath debris or located behind a wall.

1.1 Motivation

Prior radars used for vital sign estimations tend to be custom built rather than commercial radars, due to its ability to be customized. The antennas used in these systems needed to have high gain as well as low coupling between the transmitting antenna and the receiving antenna. These custom made radars tend to operate at lower frequencies, $1 - 10$ GHz, in order to maximize the tradeoff between performance and total cost of the system. At lower frequencies, these components used in these systems are cheaper and designers have much more variety to choose from.

Figure 1.2 shows vital sign systems that operate at these lower frequency bands [1][2]. From these figures, it can be seen that the size of the components along with the cables connecting them to each other, neither of these systems are portable nor lightweight. It is also clear that the antennas in these systems are large in size. Figure 1.3 shows the dimensions of an antenna that was used in a vital signs system by [1]. Operating at 6GHz, this antenna has a size of 280 mm x 130 mm, as the size of these antennas is dependent on the frequency of operation. Equation 1.1 shows the wavelength calculation.

$$\lambda = \frac{c}{f} \tag{1.1}$$

where:

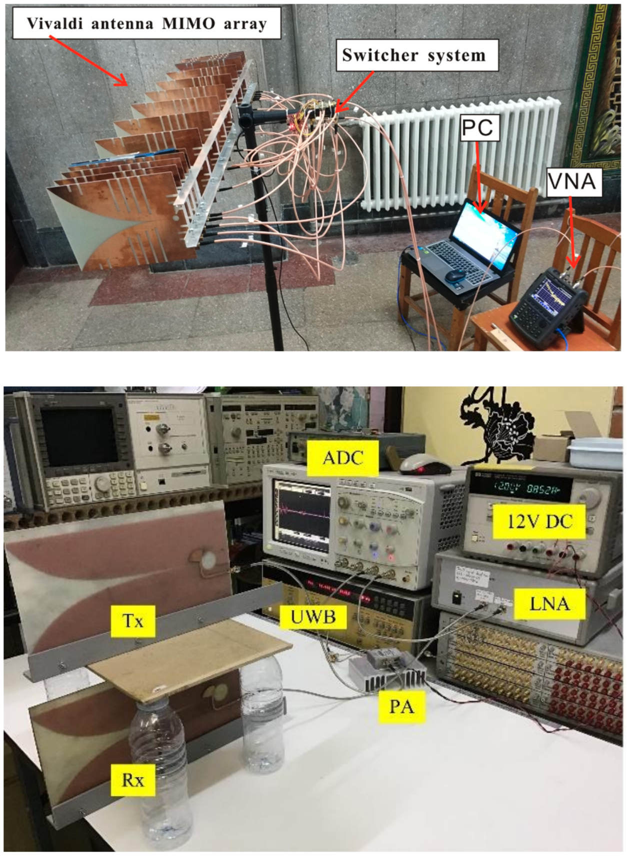

Figure 1.2: Low Frequency Vital Sign Systems

Figure 1.3: Vivaldi Antenna

λ = Wavelength

f = Frequency of Operation

c = Speed of light

For example, if a radar is needed to operate at 1GHz, using Equation 1.1, the wavelength comes out to be 0.3 m. From this wavelength, the size of the antenna is determined. Antennas are expressed in terms of wavelength. Thus, the lower the frequency of operation is, the longer the wavelength, and bigger the size of the antenna.

As mentioned previously, low mutual coupling between transmitting and receiving antennas is needed. Mutual coupling affects the efficiency of the antennas as well as their radiation pattern [3]. To combat the impact of mutual coupling, all the antenna elements should be spaced greater than half wavelength away from each other and less than one wavelength to avoid grating lobes if the mainbeam is steerable. With this spacing, as the number of antenna elements increases, so does the entire size of the system.

1.1.1 Millimeter-Wave Radars

In order to decrease the size of the radar, the operating frequency must be increased. With the development of millimeter-wave technology, antennas are now becoming smaller and smaller. Due to the millimeter-wave radars being used for autonomous vehicles, these radars are becoming more common as commercial products. With their high gain and low loss, these radars can be used for vital sign detection.

When using mmWave technology, there are two ways antennas can be implemented. The traditional way is to print the antennas, i.e. printed circuit board (PCB) on a low loss substrate. An example of this type of configuration can be seen in Figure 1.4a. While this chip is nearly 1400x smaller in area than the single antenna shown in Figure 1.3, it is still

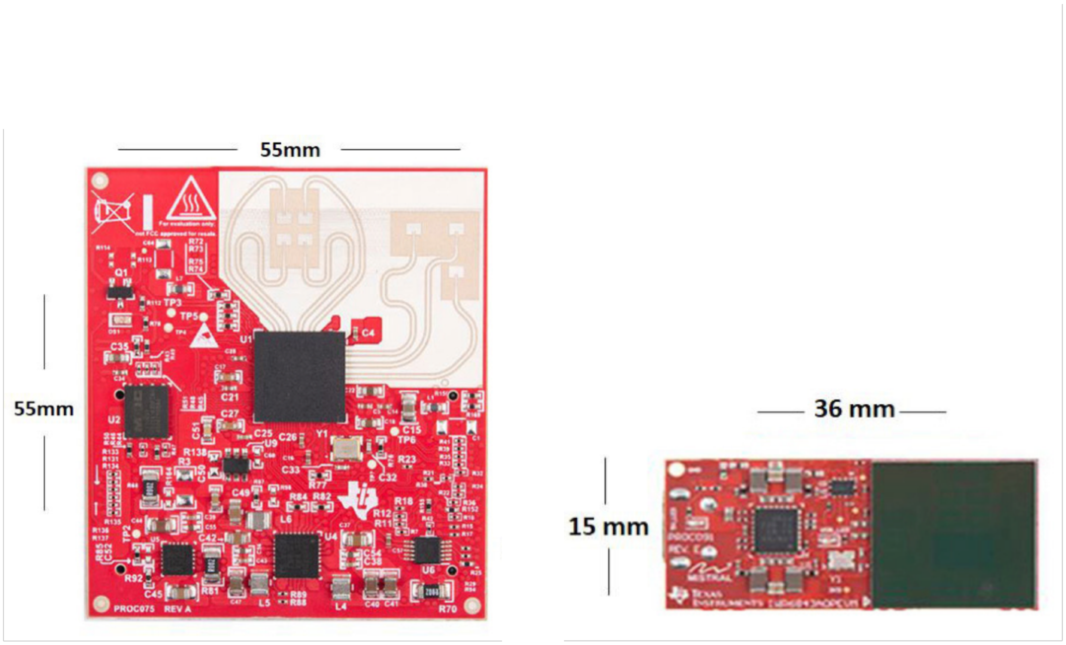

(a) TI 60 GHz Radar **(b)** TI 60 GHz Radar with AoP

Figure 1.4: mmWave Radars

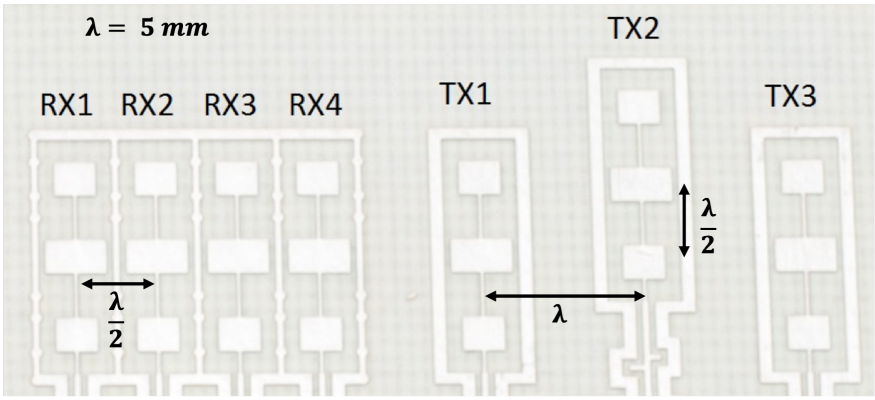

Figure 1.5: TI IWR6843 Antennas

possible to reduce the size of the board. This is possible with the use of Antenna on Package (AoP) designs. AoP is a packaging solution that allows for the antennas of a radar to be implemented onto the chip itself, rather than as a separate component [4]. This allows for the size of the entire radar system to decrease even more. An example of this type of chip can be seen in Figure 1.4b[4]. This radar is the same as the radar to it left, while also being nearly 6x smaller. Compared to Figure 1.3, the size of this entire chip is more than 7700x smaller than a single antenna on the UWB radar operating at 6 GHz.

1.2 State of the Art

Table 1.1 shows a summary of state of the art research done on vital sign detection using radars. Three different radars were used: pulse radar, continuous wave (CW) and frequency modulated continuous wave (FMCW). References [5] and [6] both use UWB radars for vital sign detection and are able to detect behind walls. [5] uses the constant false alarm rate (CFAR) algorithm to detect subjects in the field and applies the variational mode decomposition (VMD) with a grouping constraint in order to separate the heart rate pattern with the respiration rate pattern. The signal processing scheme allows for heart rate estimation of < 3 bpm with respiration rate below 1 bpm. Similar results were obtained in [6], where the vital signs were obtained by using the 2^{nd} order harmonic of the heartbeat frequency in order to recover the fundamental frequency.

Known for their simplicity and low cost, continuous wave (CW) radars have been used the longest for heart and breathing rate detection. In [7], a CW radar is used and is able to successful achieve measurements of both heart rate and respiration rate in both lying down and sitting subject scenarios. This work uses a custom peak detection algorithm to estimate the heart and respiration rates. There are also more complex algorithms that can be used to estimate vital signs, Reference [8] also uses a continuous wave radar but uses the

Table 1.1: State Of The Art Vital Sign Research

Work	Type	Signal Processing	Operating Frequency	Distance	RR Error	HR Error
Li et al.[5]	UWB	VMD	1.75 - 2.25 GHz	2.5m	0.84 bpm	2.63 bpm
Rong[6]	UWB	Adaptive 2^{nd} Harmonic Selection	7.3 GHz	1.5m	-	$<$ 2 bpm
Hanifi et al. [7]	CW	Peak Detection	24 GHz	2.5m	0.8 bpm	2.5 bpm
M. Mercuri et al.[8]	CW	WICA	5.8 GHz	2m	0.35 bpm	1.14 bpm
Ma. Mercuri et al.[9]	FMCW	Wavelet Decomposition	7.3-8.3 GHz	4m	0.24 bpm	1.43 bpm
Sacco et al.[10]	FMCW	FFT	5.8 GHz	1.5m	$<$ 1 bpm	$<$ 2 bpm
Yang et al.[11]	FMCW	FFT	60 GHz	2m	0.43 bpm	2.15 bpm

Wavelet Independent Component Analysis (WICA) technique, which is a combination of Independent Component Analysis and Wavelet Decomposition. Using this algorithm allows for higher accuracy in both heart and breathing rate detection. A FMCW radar is used in [9], [10] and [11]. Reference [9] uses direction of arrival algorithms to determine the subjects location. From this location, Wavelet Decomposition is applied to the corresponding phase signal of the subject. At a distance of up to 4 meters, heart rate error of less than 2 bpm was achieved along with a breathing rate error < 1 bpm. A similar accuracy was obtained in [10] and [11], where only a simple Fast Fourier Transform (FFT) is used on the phase signal.

1.3 Problem/Challenges

As mentioned in Section 1.1, vital sign detection has primarily been performed using large bulky radars operating at lower frequencies. However, recent developments in millimeter wave technology have allowed for development of a more portable and compact radar. While using millimeter wave radars allow for a smaller device, the use of high frequencies results in excessive loss when dealing with through wall scenarios. Figure 1.6 shows the attenuation effects of various walls vs. operating frequency of the radar. We can see that as the operating frequency increases, so does the attenuation. However, the attenuation using drywall remains relatively low at the millimeter wave range (> 30 GHz). Therefore, to avoid excessive wall loss, only drywall will be used here for through wall experiments in this work .

Additional challenges occur when detecting the heart rate of humans. The energy of the breathing signal is stronger than that of the heart. From this concept, the second and third harmonics of the breathing signal may interfere with the heart signal, which can result in inaccurate estimations. To deal with these problems, a frequency tracking algorithm, Adaptive Multi-Trace Carving (AMTC), is used to accurately estimate the vital signs of humans.

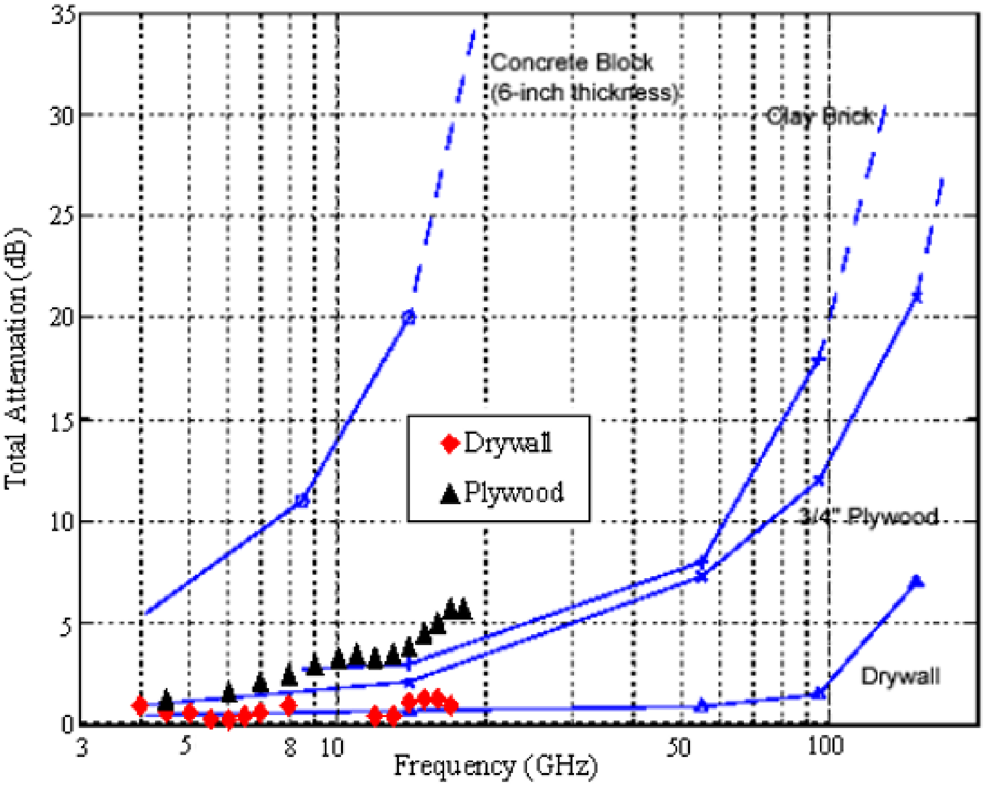

Figure 1.6: Attenuation Caused by Walls vs. Operating Frequency

1.4 Scope of Thesis

In this thesis, a compact, portable, commercial millimeter wave radar is used to detect the vital signs of humans. A breakdown of the thesis is described as follows. Chapters 2 goes over common radar systems, with a focus on FMCW radar, and breaks down their different operations. The radar used in this work is detailed here. Next, the signal processing scheme used in this work is described in detail in Chapter 3. Then, our experiments and results are presented using the millimeter wave radar are shown in Chapter 4. Chapter 5 concludes the work by showing the summary of the presented work with and a section on future work.

The objectives of this work are:

- To accurately detect the vital signs of humans using a compact, portable, commercial millimeter wave radar, and achieve comparable results to that of larger, lower frequency systems
- To develop a signal processing chain that allows the radar to detect heart and respiration rate of more than one subject
- To investigate the effects of distance, angle and drywall thickness have on vital sign detection using millimeter wave radar

1.5 Contributions

The contributions of this thesis include:

- Properly enhanced the radar capability upon utilizing MIMO and beamforming and developed the methodology to speed up its operation
- Developed a signal processing scheme to accurately detect the vital signs of humans. With a combination of super resolution direction of arrival, beamforming, and a

tracing algorithm, I was able to achieve accurate vital sign estimation, with heart rate estimation error of < 3 bpm and respiration rate error of < 1 bpm.

- Validated the algorithms by a detailed account of various scenarios in which vital signs can be accurately detected using millimeter wave radars. Various scenarios involving through wall, varying distance and angular location were performed to determine the ability and accuracy of vital sign estimation using millimeter wave radars.

1.6 Conclusion

In this chapter, vital sign detection using lower frequency radars were first discussed. The benefits of using millimeter-wave radars are then introduced. While radars previously used for vital sign detection were custom built and operated at lower frequencies, the size of the system becomes a problem when dealing with portability. With the evolution of mmWave technology and Antenna on Package solutions, portable, compact radars can now be used for vital sign estimation, while maintaining the requirements to be used for vital sign estimation.

Chapter 2

Radar Techniques

This chapter will consist of three main parts. The first part covers the basic of radar systems and three popular types of radar systems: Pulse, Continuous Wave, and Frequency Modulated Continuous Wave. Then, the FMCW radar will further be explained, primarily focused on the mathematics side of the system. Next, various antenna configurations are discussed, including Single Input Single Output (SISO) and Multiple Input Multiple Output (MIMO), with a primary focus on MIMO. Last, the radar used in this work is discussed. Various features of the radar are explained along with the communication protocol of the radar.

2.1 Radar Systems

A radar is an electromagnetic system that uses signals to detect and locate targets. The word radar is an acronym for **RA**dio **D**etection **A**nd **R**anging. This device sends out electromagnetic transmission wave and if a target is in its path, a reflected echo, or signal, will be sent back to the radar [12]. From this reflected signal, a targets distance from the radar can be determined by Equation 2.1:

$$d = \frac{cT_R}{2} \tag{2.1}$$

where:

d = Distance from Radar

T_R = Transit time of signal to travel to and back from the target

c = Speed of light

While most radars operate the same way, the type of transmitted waveform is what differentiates them from one another. There are two main wave forms: pulsed and continuous. Pulse radars operate by sending and receiving a pulse [12]. The transmitter and receiver work consecutively, so when a pulse is transmitted, the receiver is turned off, and when the receiver is waiting to detect a received signal, the transmitter will be in the off state. An example transmitted Pulse waveform can be seen in Figure 2.1.

Meanwhile, Continuous Wave (**CW**) radars, have both the receiver and transmitter operating at the same time. The transmitter is continuously sending a signal, while the receiver is on all the time. While CW radars are popular for their inexpensive cost, there are some drawbacks to using them. Due to the transmitter continuously operating, transit time cannot be calculated, thus the CW radar is unable to calculate range of the targets [13]. To combat this inability, the transmitted CW signal must be modulated in frequency. This type of system is called a Frequency Modulated Continuous Wave (**FMCW**) radar. The transmitted signal from an FMCW Radar is called a Chirp. A simple chirp is a signal that increases in frequency over time. An example of a simple Chirp can be found in Figure 2.3.

The chirp signal shown in Figure 2.3 can be mathematically expressed as [14]:

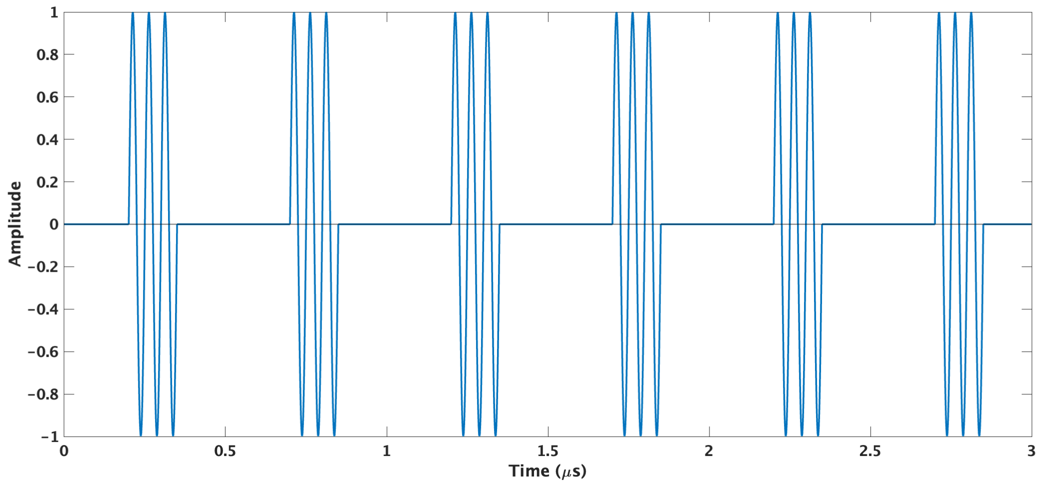

Figure 2.1: Pulse Waveform

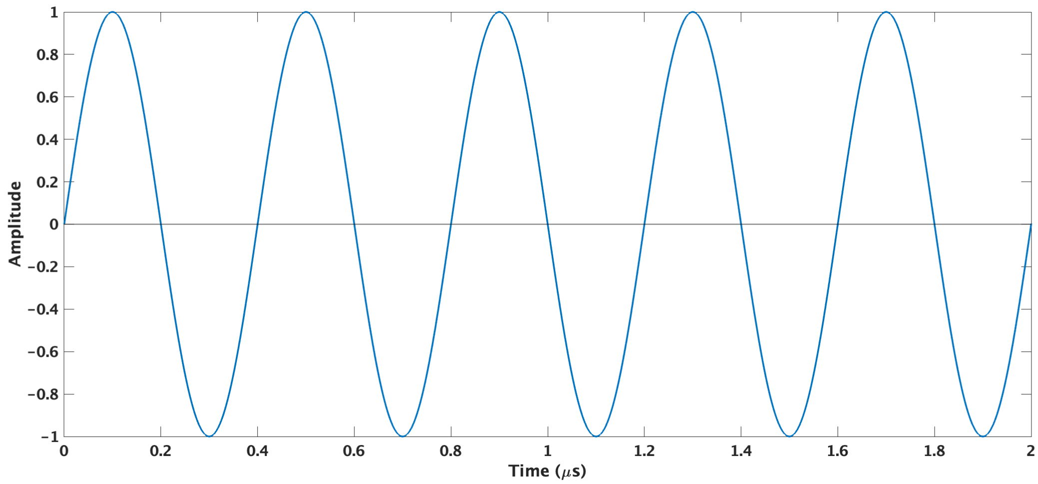

Figure 2.2: CW Waveform

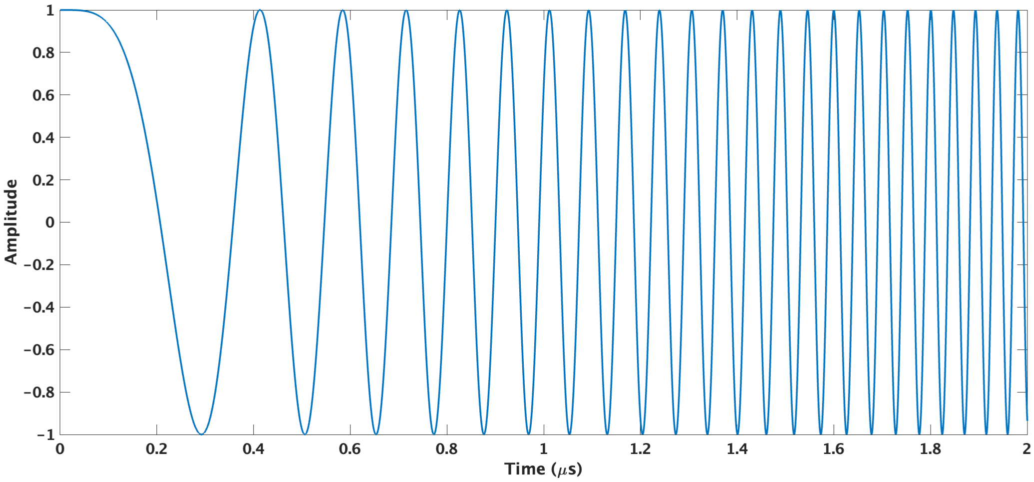

Figure 2.3: FMCW Waveform

$$x_T(t) = A_{TX}cos(2\pi f_c t + \pi \frac{BW}{T_R} t^2 + \theta(t)) \tag{2.2}$$

where:

$x_T(t)$ = Transmitted Chirp Signal

A_{TX} = Amplitude of Transmitted Signal

f_c = Starting Frequency of Chirp Signal

BW = Bandwidth

$\theta(t)$ = Phase Noise

T_R = Width of Chirp Signal Pulse

From this transmitted signal, the reflected signal, with time delay of T_R, is expressed in Equation 2.3:

$$x_R(t) = A_{RX}cos(2\pi f_c(t - T_D) + \pi \frac{BW}{T_D}(t - T_D)^2 + \theta(t - T_D)) \tag{2.3}$$

where:

$x_R(t)$ = Received Chirp Signal

A_{RX} = Amplitude of Received Signal

T_D = Time Delay

A different way of representing a Chirp can be found in Figure 2.4a. Here we can see the transmitted chirp signal and the received echo signal from a stationary target after a time delay, T_R. The transmitted chirp increases in frequency of a set sweep bandwidth, BW, over a duration, T_D. The frequency difference between the transmitted and received signals is referred to as the instantaneous beat frequency, f_b, which can be seen in Figure 2.4b. Assuming only stationary targets are located in front of the radar, the beat frequency can

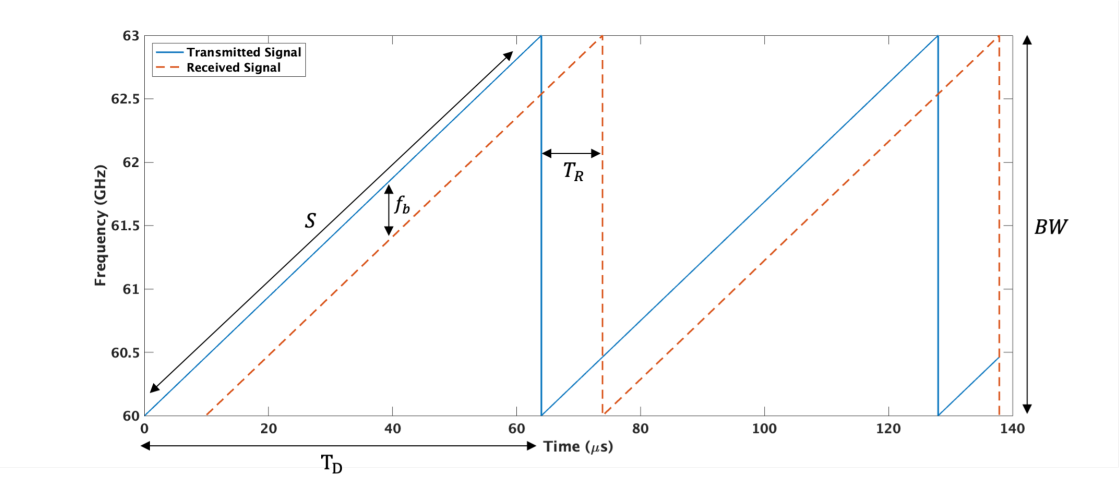

(a) FMCW Chirp

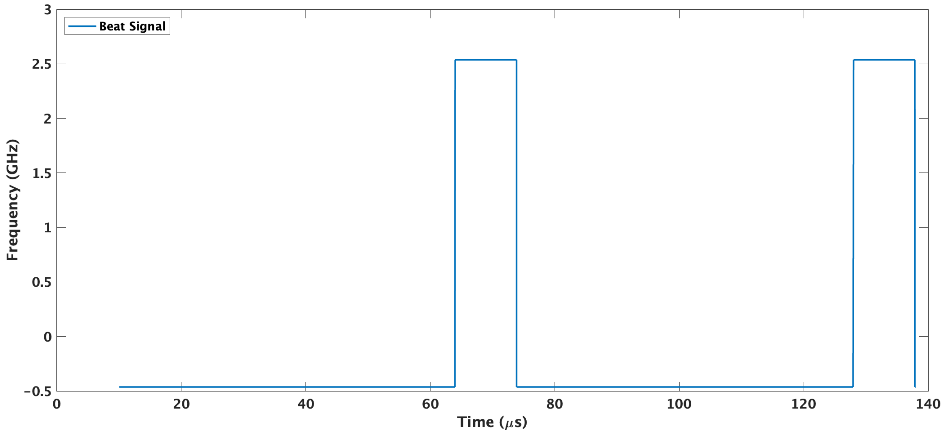

(b) Beat Signal

Figure 2.4: FMCW Signals

be shown in Equation 2.4. The carrier frequency slope, S, is the rate at which the chirps ramps up in frequency.

$$f_b = \frac{BW}{T_D} T_R = ST_R \tag{2.4}$$

where:

f_B = Beat Frequency

T_R = Transit time of signal to travel to and back from target

BW = Sweep Bandwidth

T_D = Chirp Duration

S = Chirp Ramp Speed

The beat signal can also be obtained by mixing the transmitted and reflected signal, passing the product through a low-pass filter, and sampling the signal at rate, F_s. This signal can be seen in Equation 2.5.

$$X_b(t) = A_{TX} A_{RX} e^{j(2\pi f_b t + \Psi(t))} \tag{2.5}$$

where:

$X_b(t)$ = Beat Signal

f_B = Beat Frequency

$\Psi(t)$ = Phase

Using the beat frequency, the range of the target can be determined. Combining Equation 2.4 with Equation 2.1, the range of the target can be expressed as [12]:

$$R = \frac{cT_D}{2BW} f_B \tag{2.6}$$

where:

c = Speed of Light

T_D = Chirp Duration

BW = Sweep Bandwidth

f_B = Beat Frequency

When multiple objects are located in front of the radar, multiple echo signals will be returned. There is a limit to how close these two objects can be until they can no longer be distinguished from each other. This is referred to the range/angular resolution. For an FMCW system, the range resolution is solely dependent on the bandwidth of the chirp. The greater the bandwidth, the finer the range resolution. The range resolution for an FMCW radar can be seen in Equation 2.7.

$$d_{res} = \frac{c}{2BW} \tag{2.7}$$

where:

d_{res} = Range Resolution

c = Speed of Light

BW = Bandwidth

The angular resolution is dependent on the number of channels a radar has. This concept is discussed in Section 3.2. Given a radar has N_c channels, the angular resolution can be expressed as:

$$\theta_{RES} = \frac{2}{N_C} \tag{2.8}$$

As mentioned earlier, the beat signal in Equation 2.5 is sampled at a rate of F_s. This sampling rate also limits the maximum detectable range of the radar. To calculate the maximum range of the radar, Equation 2.9 is used.

$$d_{max} = \frac{F_s c}{2S} \tag{2.9}$$

where:

d_{max} = Maximum Range
F_s = Sampling Rate
c = Speed of Light
S = Carrier Frequency Slope

Along with the ability to measure the distance of an object, radars are also capable to measure velocity. Consider the case of a person facing the radar. The person stays at a fixed distance from the radar, while also moving to their left and right. Figure 2.4a represents the transmitted signals from the radar, where two chirps are sent out and two echo chirps are received. While it is possible to calculate the range using Equation 2.6, performing a Fast Fourier Transform (**FFT**) on both chirps can also be used. This concept is known as a range-FFT and will further be discussed in detail in Section 3.1. The range FFT for each chirp will show the object at the same distance, but the phase, φ, will be different. The difference between the phases of both chirps allow for the calculation of velocity, which is shown in Equation 2.10.

$$v = \frac{\lambda \Delta\varphi}{4_D} \tag{2.10}$$

where:

v = Velocity
λ = Radar Wavelength
$\Delta\varphi$ = Phase Difference
T_D = Chirp Duration

From this concept, the maximum velocity can also be determined. Given that the velocity measurement is unambiguous if $|\varphi| < 180°$, the maximum velocity that can be measured by a radar is expressed in Equation 2.11.

$$v_{max} = \frac{\lambda}{4_D} \tag{2.11}$$

where:

v_{max} = Maximum Velocity

λ = Radar Wavelength

T_D = Speed of Light

2.2 MIMO

Classical radars have a Single Input Single Output **(SISO)** antenna configuration. A SISO radar uses a one antenna at the transmitter and one antenna at the receiver[15]. While SISO radars are used for their simplicity, multiple antennas are beneficial as it allows for an increase of angular resolution. Angular Resolution is the minimum angular separation of two objects that can be distinguished from one another. With the development of mmWave radar systems, the use of Multiple Input Multiple Output **MIMO** antenna configuration has emerged. A MIMO radar uses multiple antennas at the transmitter and receiver to send and receive signals. Each transmitted signal is orthogonal in time, which allows for a creation of a virtual array[15]. The virtual array will contain multiple channels which would contain reflected signals from each transmitter and receiver pair. The number of channels of the virtual array, N_c, is the product of the transmitters and receivers. For example, if a radar is constructed of **M** transmitters and **N** receiver, the virtual array would contain **MN** channels.

Figure 2.5 illustrates a radar system with 1 TX antenna and 2 RX antennas. Here, Angle θ represents the angle of arrival, with respect to the radar. In order for the received signal to reach receiver 2, the signal must travel a distance of $dsin(\theta)$ more than that of Receiver 1. This extra distance can be represented as a phase difference between the signals received at both RX antennas, which is calculated in Equation 2.12.

$$\omega = (\frac{2\pi}{\lambda})dsin(\theta) \tag{2.12}$$

The phase difference increases linearly as the number of receive antennas increase. Figure 2.6 shows a SIMO radar with 1 TX antenna and 6 RX antennas. Here the phase difference increases by a factor of omega across the RX antennas.

This same SIMO radar can be implemented using MIMO configuration [16]. A MIMO system with 2 TX antennas and 3 RX antennas can be seen in Figure 2.7. Here we can see that when TX1 is transmitting, the signal incoming to the three receiving elements will have a linear phase shift progression of $0, \omega, 2\omega$, respectively. Looking at TX2, since it is placed at a distance of $3d$ from TX1, its transmitted signal will travel a distance of $3dsin(\theta)$ longer than that of TX1. Because of this, the 3 receiving signals will also have a phase shift of $3d$ longer. With this longer distance, the signals received by the three receiving elements due to TX2 transmitted signal will have a phase shift of $3\omega, 4\omega, 5\omega$, respectively. Combining the receiving elements, a virtual array is created with phase difference of the channels in the following order: $0, \omega, 2\omega, 3\omega, 4\omega, 5\omega$. Comparing this radar with the SIMO radar in Figure 2.6, we are able to see that both of the phase difference sequences match up, while the MIMO radar has 3 less RX antennas and 1 more TX antenna.

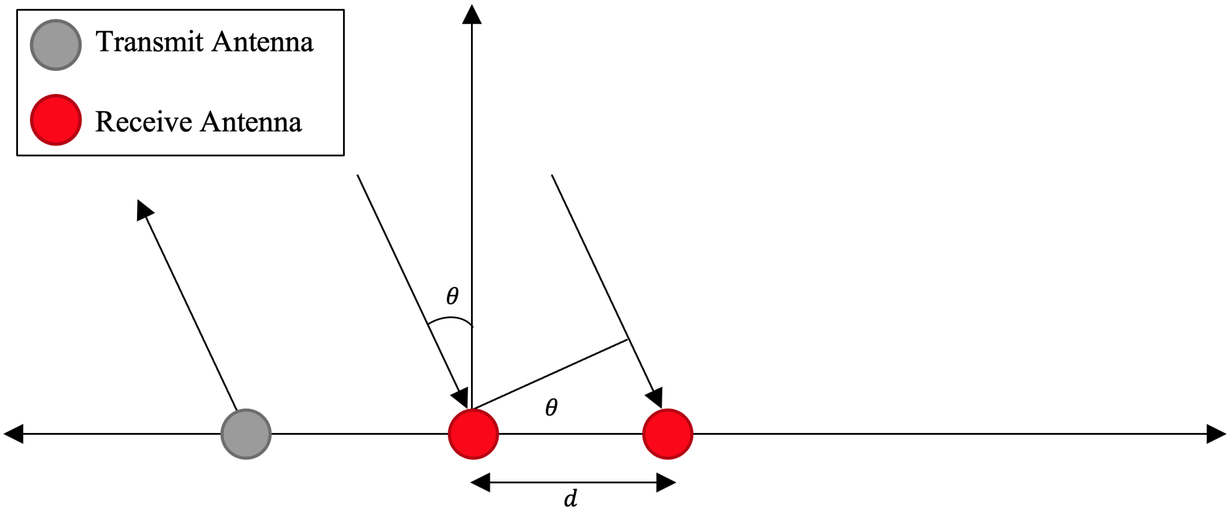

Figure 2.5: 1 TX/2 RX Configuration

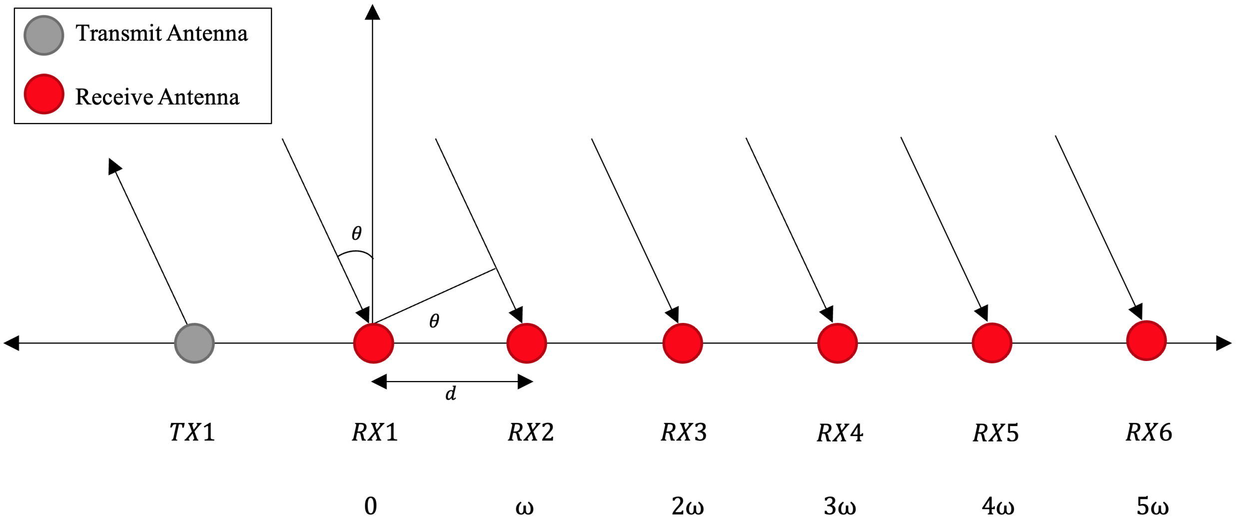

Figure 2.6: SIMO Configuration

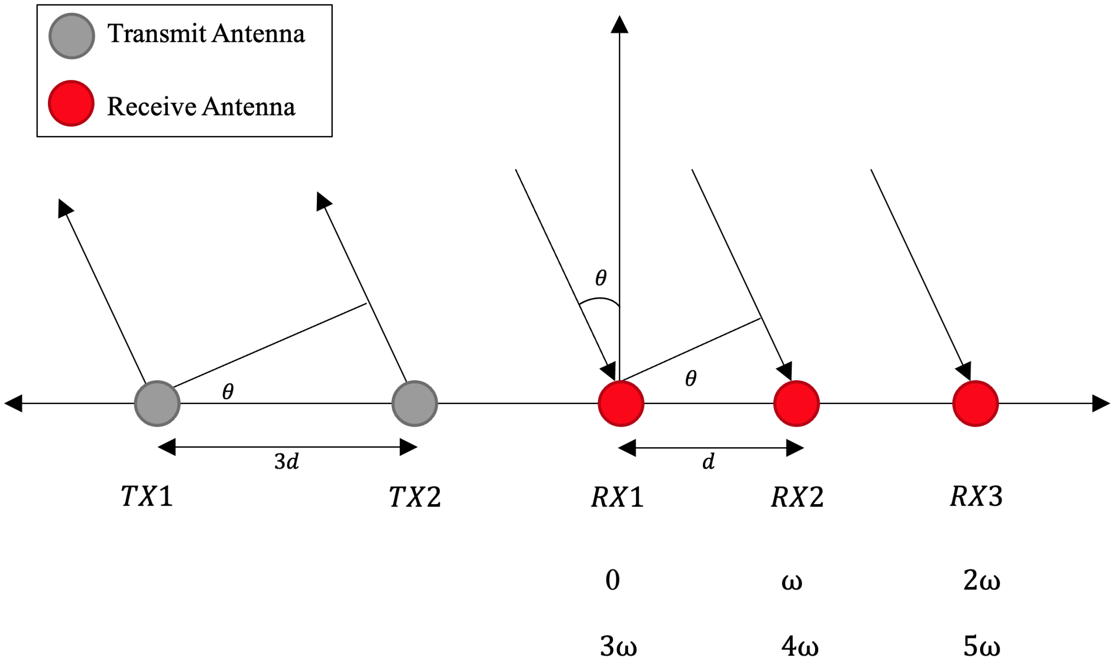

Figure 2.7: MIMO Configuration

2.3 Radar in Work

The radar used for this work is the RFbeam V-MD3 Radar, which can be seen in Figure 2.8. Operating at mmWave frequency range, 60 GHz, the V-MD3 is a commercially available, ultra-wide band FMCW radar, that allows for MIMO operation. Table 2.1 shows a breakdown of the specifications for the commercial radar[17].

This radar comes with 24 pre-configured chirp settings. These various configurations differ in maximum measuring range, frame rate, range resolution, MIMO capability, etc. These predefined settings can be seen below in Table 2.2.

Figure 2.9 shows the layout of the 3 TX and 4 RX antennas of the RFbeam. The transmit antennas are each spaced $\frac{d}{2}$ in the azimuth direction, with TX2 being placed $\frac{d}{2}$ above in elevation. All the receive antennas are also spaced out $\frac{d}{2}$. From these elements, a virtual array of the elements can be created. The $TX1$ and $TX2$ receivers are each spaced

$\frac{d}{2}$, which creates 8 antennas in a row. Since $TX3$ is $\frac{d}{2}$ above the other transmitters, its 4 receive elements are placed above the others.

The V-MD3 Radar has Ethernet connection to transfer data from the radar to the host computer. To control and communicate with the radar from the host, two protocols are used, Transmission Control Protocol (**TCP**) and User Datagram Protocol (**UDP**). TCP is known as a connection based communication method, where it first creates a reliable connection before any data packets are transferred, and will maintain the connection until all the packets are received [18]. In the case of the radar, TCP is used to configure the radar and connect/disconnect from the computer.

While similar in many ways to TCP, UDP major difference is that it is a connection-less protocol. This means that a connection does not need to be made before any data packets are transferred [18]. While a connection-less method may result in the loss of data, UDP has a data transmission speed. UDP is used to extract the data.

Figure 2.8: RFbeam V-MD3

Table 2.1: RFbeam V-MD3 Radar Specifications

Specs	V-MD3
Frequency Range	57 - 64 GHz
TX Gain	9.5 dBi
Max Sampling Rate	10 MHz
Samples/Chirp	256
Chirps/Frame	16
Range Resolution	0.05 m
Maximum Range	38.4 m
Maximum Angular Resolution	14.3 deg
Transmitters (Tx)	3
Receivers (Rx)	4

Table 2.2: Predefined V-MD3 Radar Settings

Profile	Carrier Frequency (GHz)	Sweep Bandwidth (GHz)	Sampling Rate (MHz)	Samples Per Chirp	Sweep Slope (kHz/us)	Chirps Per Frame	Frame Rate (Hz)	Range Resolution (m)	Maximum Range (m)	MIMO Enabled
#1	57	1	12	256	46875	16	100	0.15m	38.4m	No
#2	57	2	8	256	62500	16	100	0.075m	19.2m	No
#3	57	3	4	256	46875	16	100	0.05m	12.8m	No
#4	57	1	4	64	62500	16	50	0.15m	9.6m	No
#5	57	2	4	128	62500	16	50	0.075m	9.6m	No
#6	57	3	4	256	46875	16	50	0.05m	12.8m	No
#7	60	1	12	256	46875	16	100	0.15m	38.4m	No
#8	60	2	8	256	62500	16	100	0.075m	19.2m	No
#9	60	3	4	256	46875	16	100	0.05m	12.8m	No
#10	60	1	4	64	62500	16	50	0.15m	9.6m	No
#11	60	2	4	128	62500	16	50	0.075m	9.6m	No
#12	60	3	4	256	46875	16	50	0.05m	12.8m	No
#13	57	1	12	256	46875	5	100	0.15m	38.4m	Yes
#14	57	2	8	256	62500	5	100	0.075m	19.2m	Yes
#15	57	3	4	256	46875	5	100	0.05m	12.8m	Yes
#16	57	1	4	64	62500	5	50	0.15m	9.6m	Yes
#17	57	2	4	128	62500	5	50	0.075m	9.6m	Yes
#18	57	3	4	256	46875	5	50	0.05m	12.8m	Yes
#19	60	1	12	256	46875	5	100	0.15m	38.4m	Yes
#20	60	2	8	256	62500	5	100	0.075m	19.2m	Yes
#21	60	3	4	256	46875	5	100	0.05m	12.8m	Yes
#22	60	1	4	64	62500	5	50	0.15m	9.6m	Yes
#23	60	2	4	128	62500	5	50	0.075m	9.6m	Yes
#24	60	3	4	256	46875	5	50	0.05m	12.8m	Yes

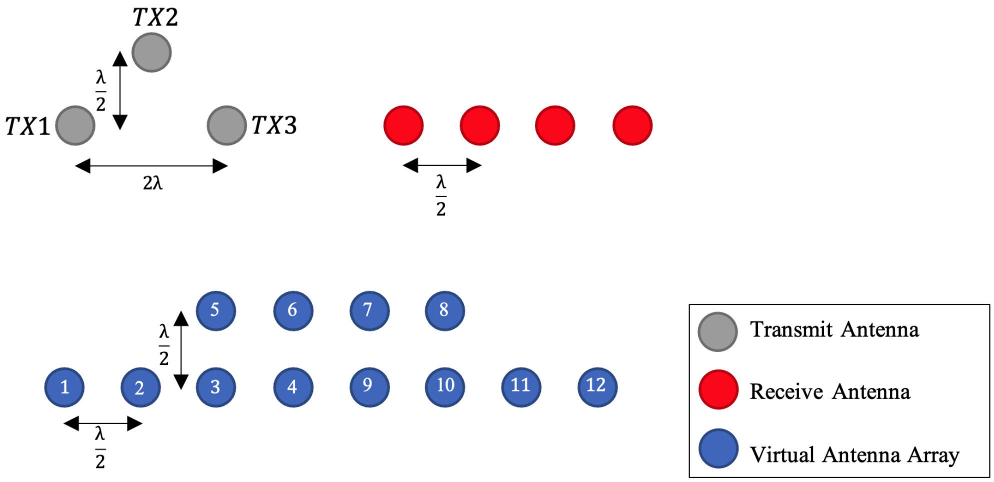

Figure 2.9: RFbeam Configuration

An example communication process is shown in Figure 2.10. Here, the TCP is used to initialize connection with the host computer and the radar. Next, the radar is configured to a specific profile chosen from Table 2.2. Once the radar settings are received, the host sends a *RDOT* message to request one frame of raw ADC data, and in return, the radar sends a completion message followed by the data from all the RX Antennas. The data here is extracted using the UDP protocol. Finally, using TCP, the host sends a message to disconnect from the radar.

Table 2.3 shows other current state of the art mmWave radars. All of the radars included allow for MIMO capability and operate using FMCW technology. Compared to these radars, the V-MD3 uses Antenna on Package technology to allow the antennas to be directly located on the radar chip. This allows for the size of the radar to be smaller than other millimeter wave radars.

2.4 Conclusion

In this chapter, the basics of radar theory was introduced. The background of FMCW radar systems was shown, including the ability to measure range and velocity of objects. The benefits of using MIMO antenna configurations were then discussed followed by the introduction of the radar used in this work, the V-MD3 radar. With a better understanding of mmWave FMCW systems with MIMO antenna configuration, the signal processing scheme used in this work can now be discussed.

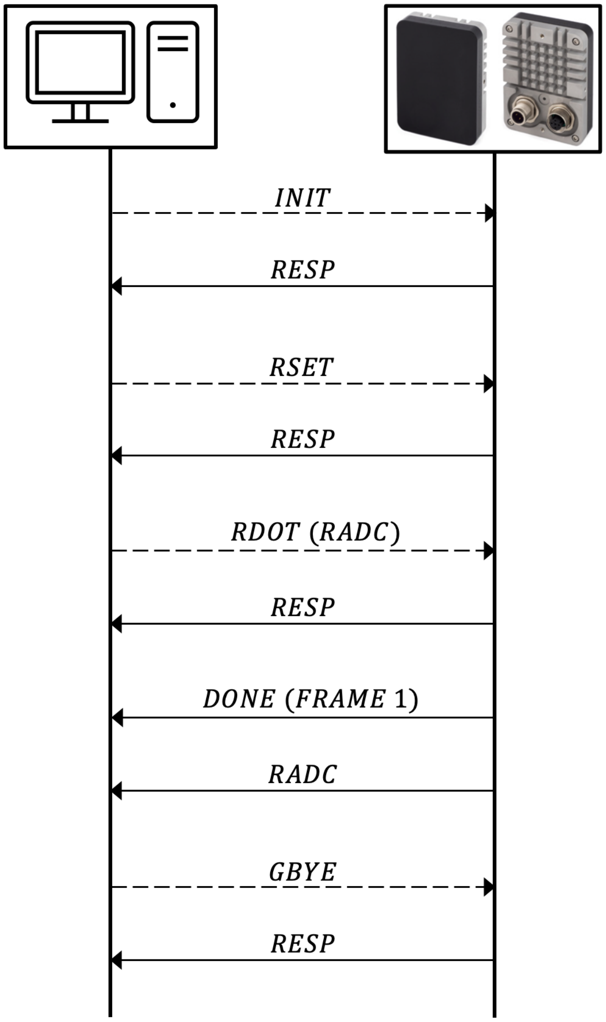

Figure 2.10: Host & Radar Communication

Table 2.3: Current State of Art mmWave Radars

Manufacturer	Type	Frequency	Tx Antennas	Rx Antennas
Jorjin Technologies	FMCW	61-61.5GHz	1	3
Texas Instruments (TI)	FMCW	60-64GHz	3	4
Jorjin Technologies	FMCW	60-64GHz	3	4
Infineon	FMCW	58-63.5GHz	1	3
Texas Instruments (TI)	FMCW	77-81GHz	12	16
Colorado Engineering	FMCW	60-64GHz	3	4

Chapter 3

Software

The chapter discusses the signal processing scheme used to extract vital signs using radars. The importance of each step in the processing chain for heart and respiration rate estimation is shown. The following main parts of the processing chain will be discussed: Range Profile, Direction of Arrival, Digital Beamforming, Phase Variation, and the heart rate and respiration rate extraction algorithms.

The processing chain used in this work can be seen in Figure 3.1. First, the beat frequency signal from each virtual channel is demodulated and sampled by the ADC of the radar, into a $I + jQ$ complex time domain signal with a length noted by *Samples.* For each chirp recorded, the data is appended to each other to form a 2-Dimensional Array. The data from all channels is then organized into a radar cube, with dimensions *Samples x Chirps x Channels.* This process is illustrated below in Figure 3.2.

3.1 Range Profile

As discussed in Section 2.1, the beat signal contains the range information of the target. This beat frequency is contained in the sampled time domain signal. To obtain the

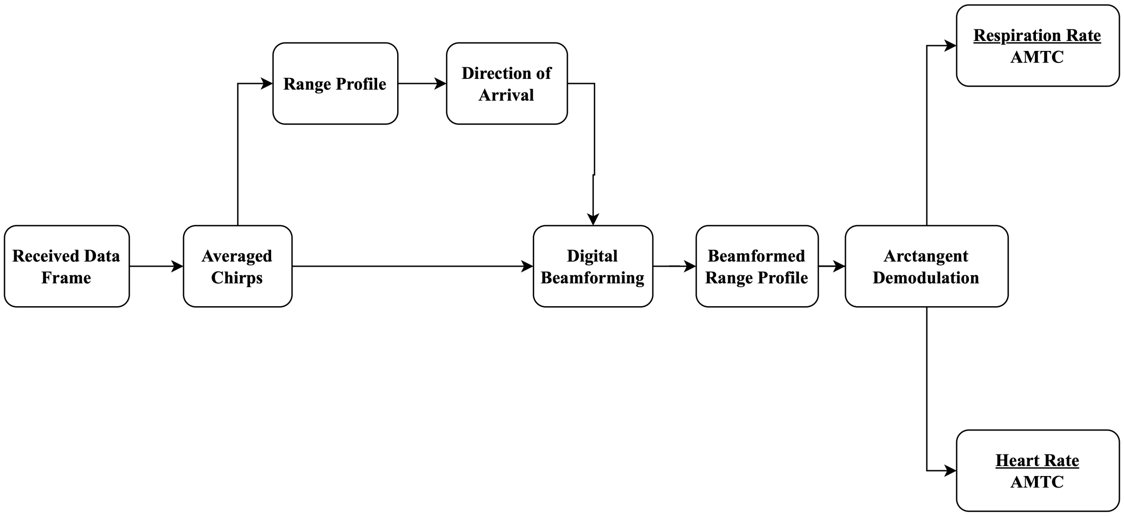

Figure 3.1: Signal Processing Chain

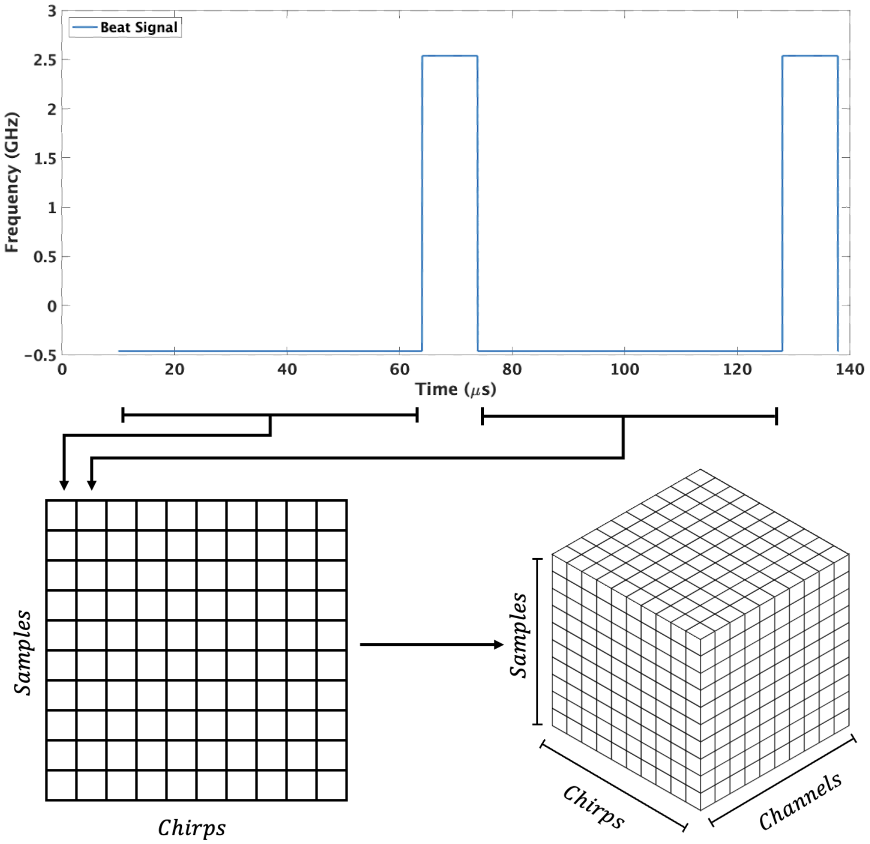

Figure 3.2: Received Data Frame

range of the target, the radar cube is transformed into the frequency domain by using an Inverse Fast Fourier Transform (IFFT) across the *Samples* dimension. Figure 3.3 shows the transformation of the radar cube. By performing the IFFT, the spectrum will contain peaks at various frequencies that represent the range bin at where the target is located. The higher the frequency, the further the target is from the radar. For each frequency, there is a corresponding range bin that is set for each predefined radar processing settings

An example range profile of a single target can be seen in Figure 3.4. Here we can see that the subject is stationary and located predominantly at Range Bin 30. The V-MD3 radar has a range bin resolution of 0.05m, which means that the target is located at 1.5m.

3.2 Direction of Arrival

Following the range profile estimation, subject localization is needed to determine the exact location of the target from the radar. To do this, direction of arrival (**DOA**) methods are used. The background of direction of arrival and various algorithms are discussed further in detail later in this section. Using DOA, a map can be made of the entire field of view to identify any targets that are located in front of the radar. An example map using the MUSIC Algorithm can be seen in Figure 3.5.

3.2.1 Background

In order to perform any DOA estimation, a radar must consist of at least two receiving elements. MIMO radars have a large array of antennas. Therefore, a MIMO radar has the ability to calculate direction of arrival. Direction of arrival is important as it allows the angular location of a signal source to be determined, as well its location in both cross range

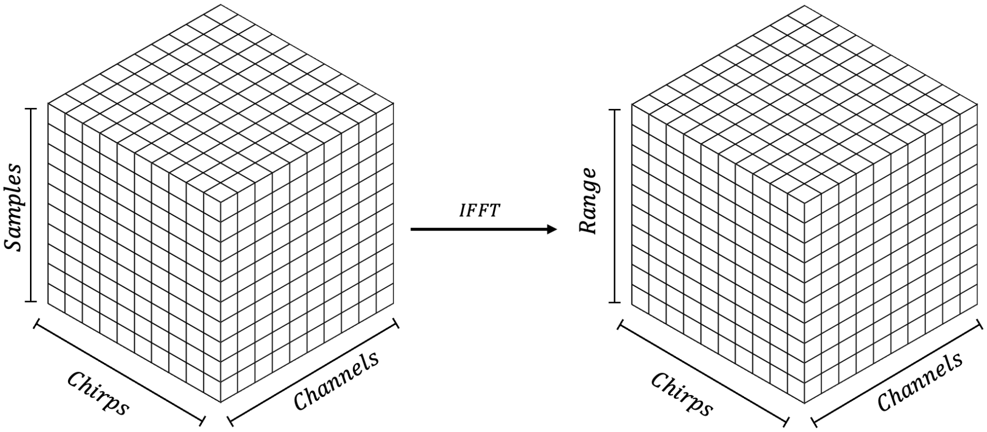

Figure 3.3: Range FFT

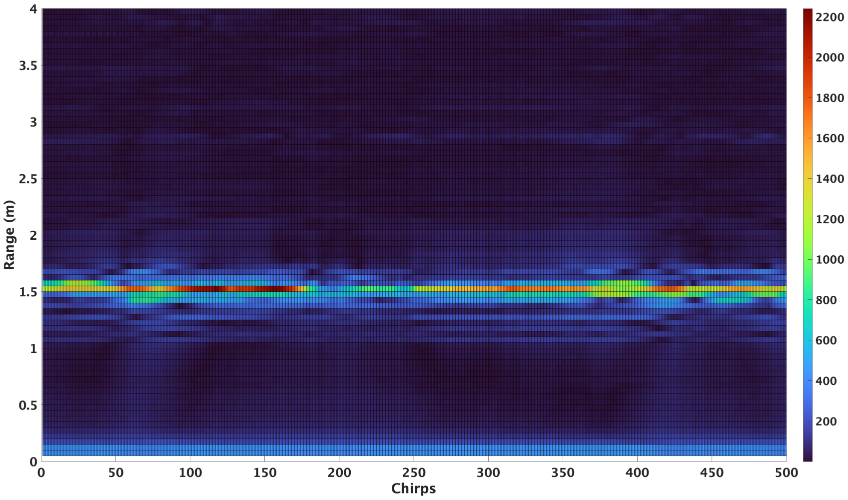

Figure 3.4: Range Profile

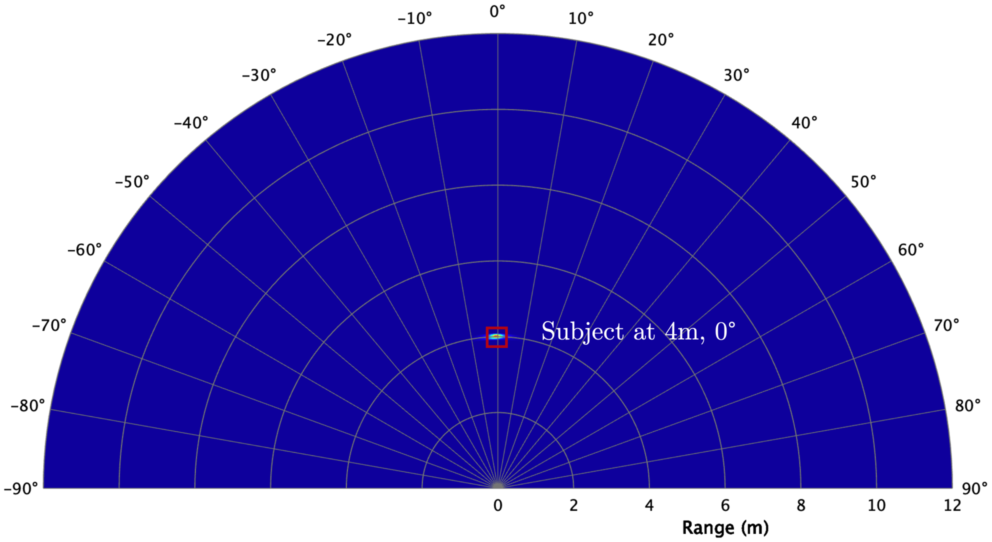

Figure 3.5: Range Map

and down range. Narrowing down this angle is important as it allows for the separation of the signal of interest from noise and interference from other signals.

As mentioned in Section 2.2, for a MIMO radar system, every additional channel will induce a phase shift. From this phase shift, an estimated angle of arrival can be calculated from Equation 3.1 [19].

$$\theta = sin^{-1}(\frac{\omega\lambda}{2\pi d}) \tag{3.1}$$

where

ω = Phase Shift

λ = Center Frequency Wavelength

d = Distance between Elements

As the number of channels, N_C, increases, the number of phase shifts also increase to $N_C - 1$. To estimate the DOA when $N_C > 2$, an FFT is performed across the phase shifts [16]. This is referred to as an Angle FFT. Figure 3.6 shows Angle FFT Direction of Arrival estimations for two objects at the same range located at $-15°$ and $+15°$. Here we have two cases, one when $N_C = 2$ and another with $N_C = 8$. From this figure, it can be seen that the case of $N_C = 2$ is unable to differentiate between the two objects while the other case of $N_C = 8$ is able to. This is the concept of angular resolution, the ability for a device to distinguish and separate two equal sized objects that are the same range away from the radar. Given the antenna spacing is $\frac{\lambda}{2}$, the angular resolution can be calculated by Equation 3.2. This equation shows that as the number of channels increases, the finer the angular resolution becomes. For the V-MD3 Radar, the azimuth angular resolution is calculated out to be 14.3° and the elevation angular resolution is 26.4° .

$$\theta_{RES} = \frac{2}{N_C} \tag{3.2}$$

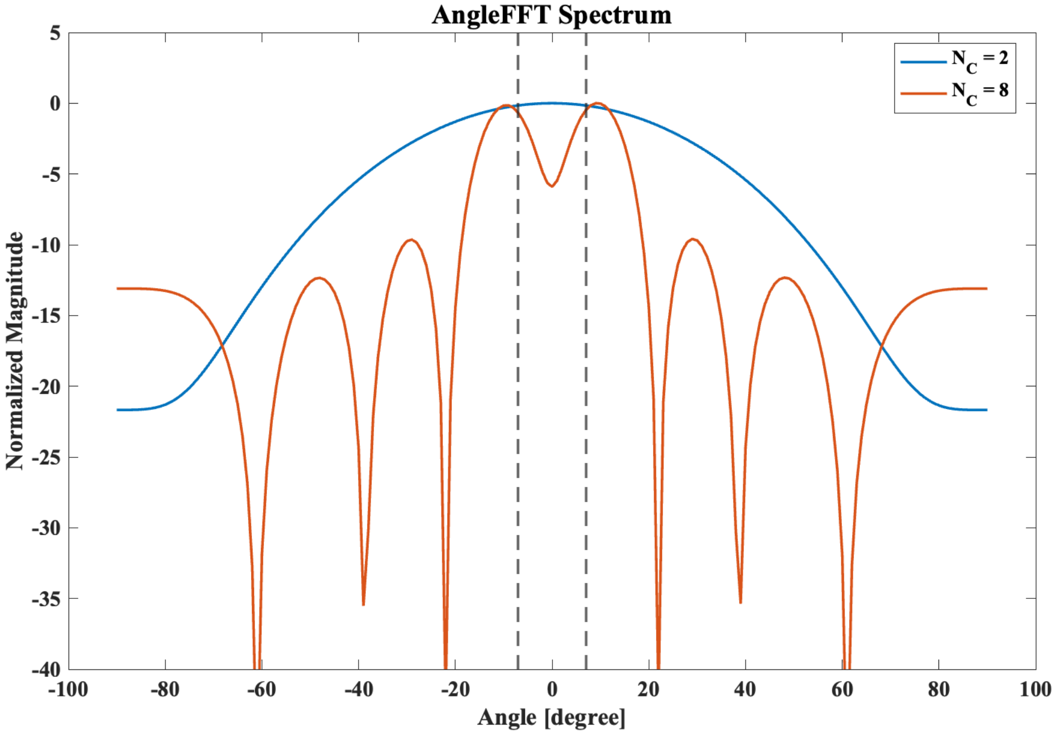

Figure 3.6: Angle FFT Estimation

To perform any high resolution DOA techniques, a background of received signals must be understood. As mentioned previously in Section 2.2, we showed how every additional channel of a MIMO system will have a phase shift and how all received signals will contain both the signal of the source combined with noise from the environment. Looking at Figure 2.9, let the source signal arriving into Virtual Array Channel #1 be $s_k(t)$. From the initial received signal, we are able to use Equation 3.3 to determine the source signal traveling to the mth element of the array [19]. This spatial frequency μ is what allows us to find the Direction of Arrival of a source. For every spatial frequency, there is a corresponding DOA angle [19]. The spatial frequency has a range of $-\pi \leq \mu \leq \pi$, which corresponds to a DOA range of $-90 \leq \theta \leq 90$.

$$s_{km}(t) = s_k(t)e^{j(m-1)\mu_i} \tag{3.3}$$

where:

s_{km} = Source Signal to mth receive element

k = source/object

m = Receiving Element

μ = spatial frequency

From this concept, we are now able to calculate the received signals from all channels. For every K^{th} object, or signal source, detected in a radar scan, the signal received by the mth RX element can be expressed as in Equation 3.4[19]:

$$x(t) = \sum_{k=1}^{K} s_k(t)e^{j(m-1)\mu_i} + n_m(t) = \sum_{k=1}^{K} a(\theta_k)s_k(t) + n_m(t) \tag{3.4}$$

where:

$x(t)$ = Received Signal
s_k = source signal
n_m = Noise & Interference Signal
$a(\theta_k)$ = array steering vector

Here the array steering vector, $a(\theta_k)$, is a vector of phase shifts, $e^{j(m-1)\mu_i}$, with spatial frequency ranging from $[-\pi, \pi]$. Equation 3.4 can be written in a matrix form as the following.

$$X(t) = AS(t) + N(t) = \sum_{k=1}^{K} a(\theta_k)s_k(t) + n_m(t) \tag{3.5}$$

where:

$X(t)$ = Received Data Matrix
A = Array Steering Matrix: $[a(\mu_1)\ a(\mu_2)\ a(\mu_3)\ \ldots\ a(\mu_K)]$
$S(t)$ = Source Signal Vector: $[s_1(t)\ s_2(t)\ s_3(t)\ \ldots\ s_M(t)]$
$N(t)$ = Noise & Interference Signal Vector $[n_1(t)\ n_2(t)\ n_3(t)\ \ldots\ n_M(t)]$

For all the channels in a radar, the source signals are correlated as they are reflecting off the same object, while the noise signals will be uncorrelated as they are due to the environment [19]. From this concept, direction of arrival estimations can be extracted by constructing a covariance matrix of the Received Data Matrix. This covariance matrix is expressed in Equation 3.6. Given the range bin estimation from the range profile, the matrix $X(t)$ is made up of the corresponding slice from the radar cube. An example can be seen below in Figure 3.7. This covariance matrix will be used in the direction of arrival algorithms that are described in this work.

$$R_{xx} = \frac{1}{N}\sum_{n=1}^{N}[x(t)x^H(t)] = \frac{1}{N}X(t)X^H(t) \tag{3.6}$$

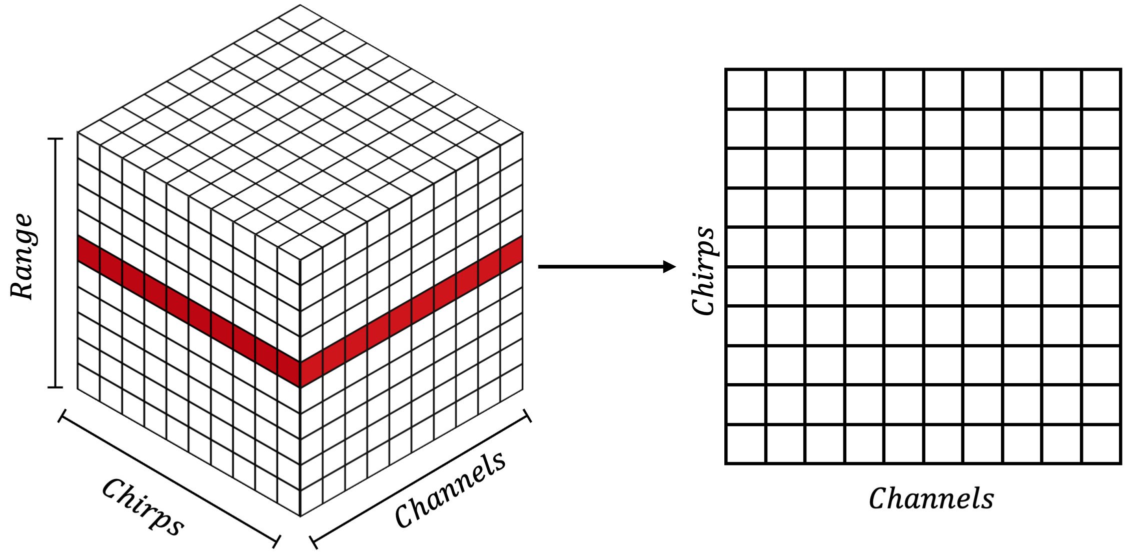

Figure 3.7: Direction of Arrival Input Matrix

where:

R_{xx} = Covariance Matrix

$x(t)$ = Received Signal

N = Number of Chirps

$X(t) = [x(t_1)\ x(t_2)\ x(t_3)\ \ldots\ x(t_N)]^T$

3.2.2 Algorithms

The most common technique for DOA estimation is the use Conventional Beamforming **CBF**. Beamforming techniques have been used for their low complexity and easy implementation [20]. As will be discussed in Section 3.3, CBF techniques involve the use of antenna array steering vector, $a(\theta)$, in order to scan across an angular region to locate where the maximum output power occurs [20]. These locations are the direction of arrival of signal sources.

From this weighted signal, the total output power can be calculated from Equation 3.7:

$$P(w) = \frac{1}{N}\sum_{n=1}^{N}[|y(t_n)|^2] = \frac{1}{N}\sum_{n=1}^{N} w^H x(t_n) x^H(t_n) w \tag{3.7}$$

Weight vector w can be normalized to $\frac{a(\theta)}{\sqrt{a^H(\theta)a(\theta)}}$. Combining Equation 3.7 with Equation 3.6, the total output power can be expressed as a function of θ by:

$$P(\theta) = \frac{a^H(\theta)R_{xx}a(\theta)}{a^H(\theta)a(\theta)} \tag{3.8}$$

While conventional beamforming is popular for its simplicity, problems occur when multiple source signals are present. The CBF output will show sources from the correct angle as well as other sources. To deal with this problem, an adaptive version of beamforming called the Minimum Variance Distortionless Response (**MVDR**) algorithm was constructed.

Created by Jack Capon, the MVDR algorithm creates and steers a beam in one direction to find maximum output power, while nulling the signals from other directions [19]. These nulls are formed by constraining the steered beam in the looking direction. This expression is mathematically expressed below:

$$\min P(w) \text{ subject to } w^H a(\theta) = 1 \tag{3.9}$$

From this constraint, the weight vector for this algorithm is obtained as:

$$w = \frac{R_{xx}^{-1} a(\theta)}{a^H(\theta) R_{xx}^{-1} a(\theta)} \tag{3.10}$$

where:

w = Weight Vector

R_{xx} = Covariance Matrix

$a(\theta)$ = Array Steering Vector

By inserting Equation 3.10 into Equation 3.8, the Output Power Spectrum of the MVDR algorithm can be expressed as:

$$P_{MVDR}(\theta) = \frac{1}{a^H(\theta) R_{xx}^{-1} a(\theta)} \tag{3.11}$$

An example case comparing the CBF and the MVDR algorithm can be seen in Figure 3.8. This example is of an 8 channel radar with two signals at $-5°$ and $+5°$. Here, we can see that while the CBF algorithm is unable to distinguish between the signals due to high angular resolution, the MVDR algorithm has two clear peaks at both of the expected angles.

The second main technique used for Direction of Arrival estimation are subspace based methods [21]. Subspace methods allow for higher resolution and higher accuracy estimates by the use of eigenvalue decomposition on the covariance matrix. These methods start by

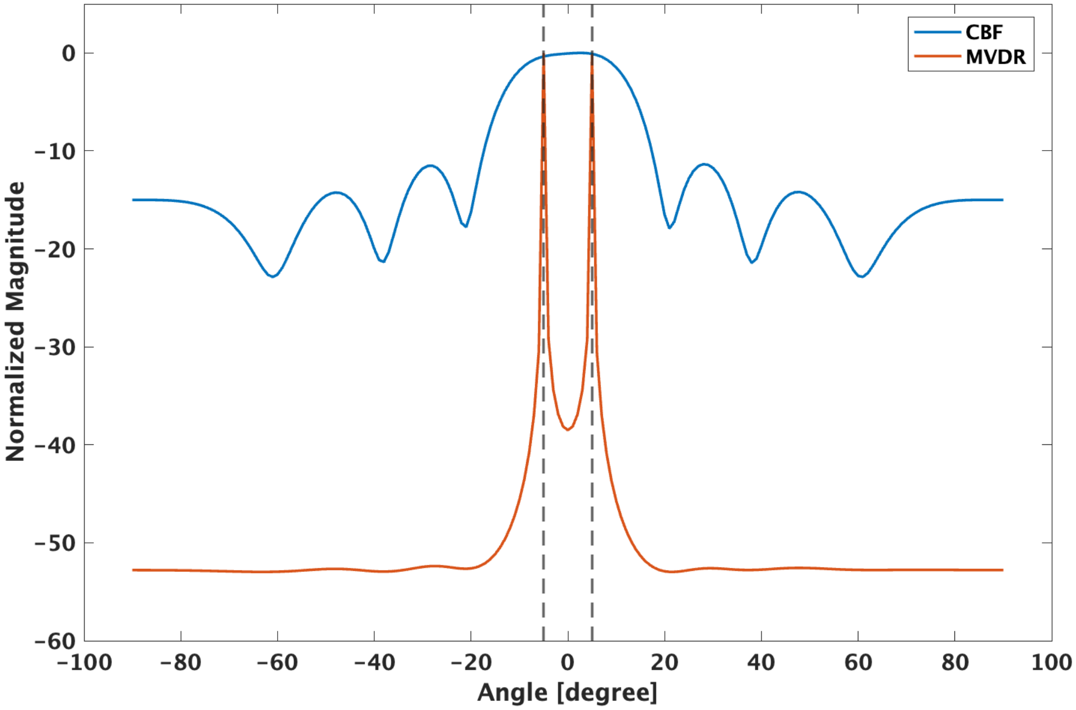

Figure 3.8: Direction of Arrival Comparison

letting the Received Data Matrix, $X(t)$, form a received signal vector space, with vector dimension of N_C channels. As mentioned in Equation 3.4, a received signal can be broken into two parts: the source signal and noise. Thus, the received signal space can be separated into a source signal subspace and noise subspace. The signal subspace is the subspace spanned by the columns of Array Steering Matrix, which is defined in Equation 3.5, and the noise subspace is the subspace orthogonal to the signal subspace. Since these two subspaces are orthogonal to each other, subspace based algorithms are able to utilize this identity to estimate the direction of arrival [19].

One of the most commonly used subspace methods is the Multiple Signal Classification (**MUSIC**) algorithm. With its ability to be used for azimuth and elevation direction of arrival estimation alongside with range approximation, MUSIC is one of the most popular high resolution algorithms. The MUSIC algorithm uses eigen-decomposition to isolate the noise and signal subspace[19]. First, the covariance matrix from Equation 3.6 can be rewritten as the following:

$$R_{xx} = AR_{ss}A^H + \sigma_n^2 I_M \tag{3.12}$$

where:

R_{xx} = Covariance Matrix

A = Array Steering Matrix

R_{ss} = Signal Correlation Matrix

σ_n^2 = Noise Common Variance

I_M = Identity Matrix with Rank M

Next, eigenvalue decomposition is performed on the covariance matrix. Let $[\lambda_1 \; \lambda_2 \; \ldots \; \lambda_M]$ be the eigenvalues, where $[\lambda_1 \geq \lambda_2 \geq \cdots \geq \lambda_M]$ and matrix Q contain the corresponding eigenvectors, V, of the covariance matrix such that:

$$|R_{xx} - \lambda_i I_M| = |AR_{ss}A^H + \sigma_n^2 I_M - \lambda_i I_M| = 0 \tag{3.13}$$

From these eigenvalues, the number of sources can be determined by finding the multiplicity of the smallest eigenvalue. This value can be found by Equation 3.14:

$$d = M - K \tag{3.14}$$

where

d = Number of Sources

M = Number of Channels

K = Multiplicity of Smallest Eigenvalue

Then, we need to determine the signal subspace and noise subspace. The eigenvectors are able to be separated into signal and noise eigenvectors where:

$$Q_s = Q[V_1 \ldots V_d] \quad Q_n = Q[V_{d+1} \ldots V_M] \tag{3.15}$$

where:

Q_s = Signal Subspace

Q_n = Noise Subspace

V = Eigenvectors of Covariance Matrix

d = Number of Sources

M = Number of Channels

From the noise subspace, the power spectrum of the MUSIC algorithm can be calculated using Equation 3.16.

$$P_{MUSIC}(\theta) = \frac{1}{a^H(\theta) Q_n Q_n^H a(\theta)} \tag{3.16}$$

where:

$P_{MUSIC}(\theta)$ = MUSIC Power Spectrum

R_{xx} = Covariance Matrix

$A(\theta)$ = Array Steering Vector

Q_n = Noise Subspace

An example case of the MUSIC algorithm can be seen below in Figure 3.9. This example is of a 8 channel radar with two source at $-15°$ and $+15°$. The MUSIC algorithm is able to clearly able to distinguish the sources, with two clear peaks at the expected angles. Table 3.1 shows a comparison of the different algorithms. While the MUSIC algorithm has a longer computation time than both MVDR and CBF algorithms, the estimations are much more accurate. To get high accuracy results with a short computation time, I developed a combination of MVDR and MUSIC to speed up the response. Using MVDR, an estimation can be made of both the number of subjects in the field of view as well as the angle and range of each subject. Using these estimates, we can use the MUSIC algorithm to calculate a more precise estimation. By limiting the array steering matrix to search only around the estimated angle by setting a threshold, the computational time of the MUSIC algorithm was decreased.

3.3 Digital Beamforming

A radars field of view can be defined as the farthest angle that a radar can estimate a direction of arrival, both to its left and right. This value is determined by the distance, or spacing, between two antenna elements. From this spacing, the maximum field of view can be calculated as:

$$\theta = sin^{-1}(\frac{\lambda}{2d}) \tag{3.17}$$

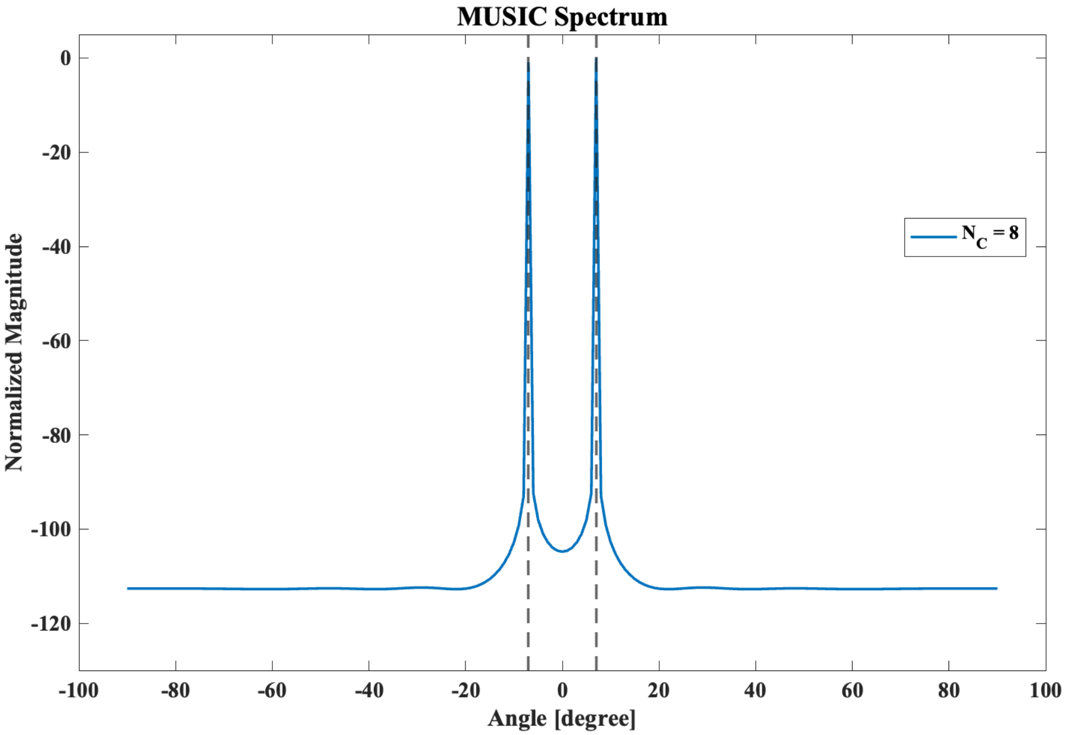

Figure 3.9: MUSIC DOA Comparison

Table 3.1: Comparison of Direction of Arrival Algorithms

Algorithm	Computation Time	Angle Accuracy
CBF	0.109s	±9°
MVDR	0.111s	±6°
MUSIC	0.274s	±3°
MVDR + MUSIC	0.133s	±3°

where

λ = Center Frequency Wavelength

d = Spacing between Elements

In this work, the V-MD3 radar has a spacing of $\frac{\lambda}{2}$, which yields a field of view of ± 90°. For this wide angular field of view, to isolate the individual subjects from each other, some

type of scanning is required. While some radars allow the possibility to mechanically steer an antenna, fixed antennas can be steered digitally. This is known as Digital Beamforming. Digital Beamforming is a commonly used signal processing technique as it allows for the extraction of a source signal of interest from the noise and interference of the environment [20]. This is different than analog beamforming, which uses analog phase shifters on the antenna in order steer the antennas. By applying a weight vector, w_n, the beam of an antenna array can be steered into any particular direction. An visual example of beam steering can be seen in Figure 3.10. The beam can originally be seen to be directed at 0°. If it is determined the subject is located 30° left of the radar boresight, then weights can be added to the individually received signal mathematically. An example of the digitally steered beam can be seen in Figure 3.10b, when the beam is steered to 30 degrees. This concept of beamforming can be expressed in Equation 3.18. To simplify the notation, the conjugate of the weight vector is used.

$$y(k) = \sum_{n=0}^{N_c-1} w_n^* x_n(k) \tag{3.18}$$

where:

y_k = Beamformed Signal

w_n = Weight Vector

$x_n(k)$ = Received Signal from Channel n

N_c = Number of Channels

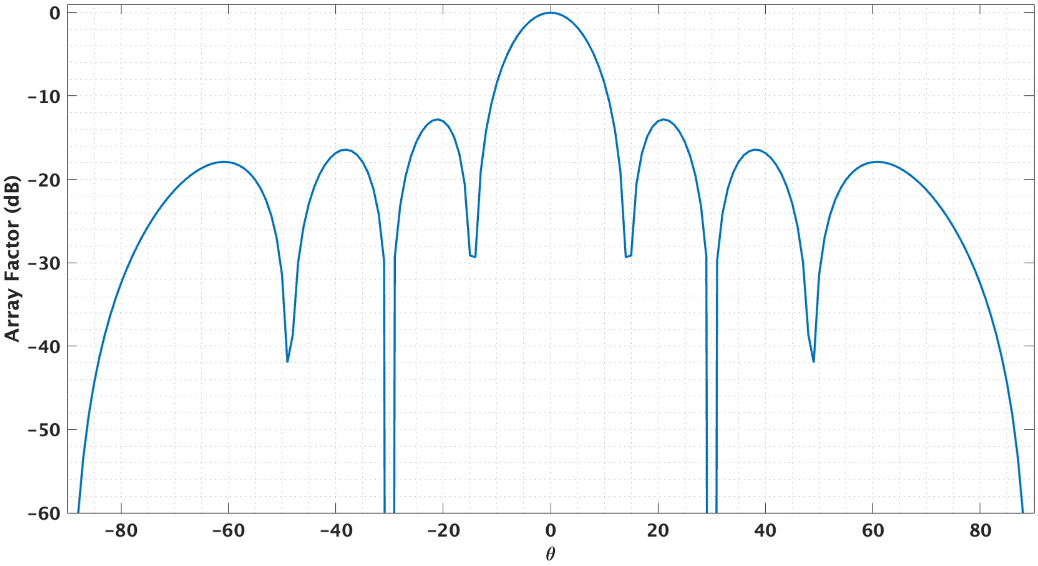

(a) Beam at 0°

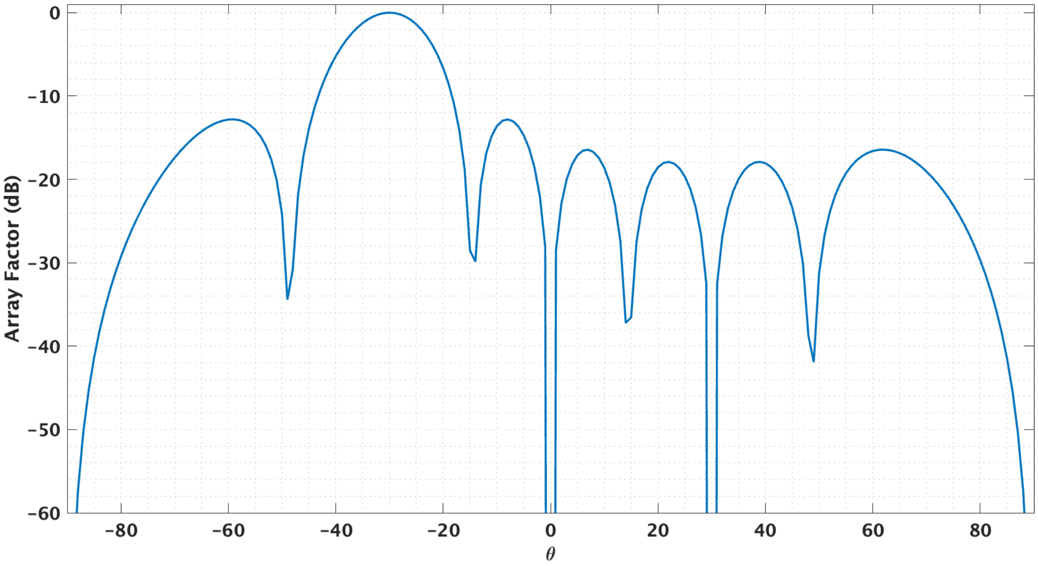

(b) Beam at 30°

Figure 3.10: Beam Steering

A visual expression of beamforming can be found in Figure 3.11. The prescribed radar consists of N_C number of channels. For each channel of the radar, a weight vector is applied. Then, the sum of these weighted channels are calculated to create a single beamformed channel.

From our DOA estimation methods, the azimuth locations of each subject in the scene will be identified, which is defined as angle θ. For each angle θ identified, the weight vector will need to be calculated and applied to the original radar cube, $x(k)$, resulting in $y_m(k)$ where $m = 1 - M$ and M is the number of subjects. Given that the V-MD3 radar has a spacing of $\frac{\lambda}{2}$ between receive antennas, the weight vector can be calculated using Equation 3.19.

$$w_n = e^{-jk_0 dnsin\theta} = e^{-j\pi nsin\theta} \tag{3.19}$$

where:

w_n = Weight Vector

k_n = free-space wavenumber

d = Spacing Between Elements

3.4 Phase Variation

Once the radar cube has been steered in the direction of the subject, the phase variation can be extracted. Arctangent Demodulation is a phase based method which extracts the phase of the I/Q signals over the range profile. By using this method, the physical movement can be extracted to signal $\psi(t)$. From this signal, both the movement of the breathing and heart can be calculated. To perform the Arctangent Demodulation, a range FFT is performed on the steered beamformed channel. Then, since the range of the subject is already known, the

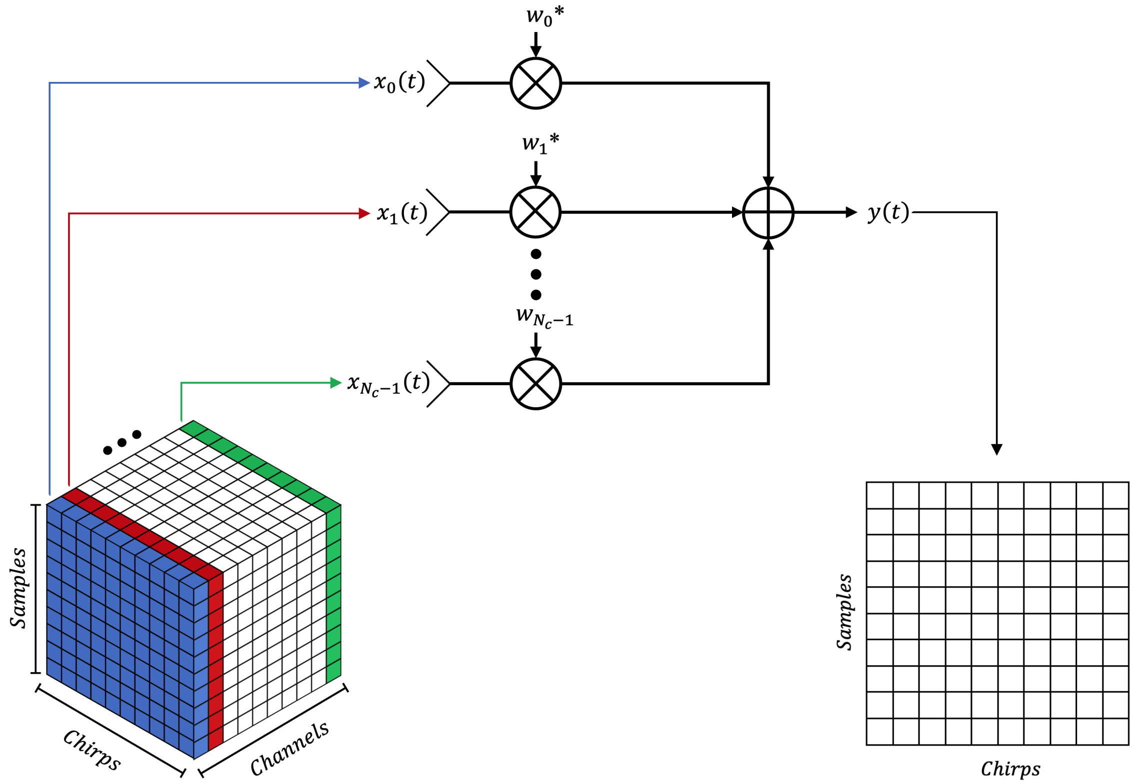

Figure 3.11: Beamforming of Radar Cube

row with the corresponding range bin is extracted, which can be expressed as $B(t)$. The demodulated signal $B(t)$ can then be broken into its I and Q channels as [14]:

$$\begin{aligned} B_I(t) &= A_I cos(2\pi f_b n T_M + \Psi_l(t)) + DC_I \\ B_Q(t) &= A_Q cos(2\pi f_b n T_M + \Psi_l(t)) + DC_Q \end{aligned} \tag{3.20}$$

where:

$B_I(t)$ = Imaginary Channel of B(t)
$B_Q(t)$ = Real Channel of B(t)
DC_I = DC Offset
DC_Q = DC Offset

Arctangent demodulation is then performed using Equation 3.21. Variable F is added to deal with phase discontinuities, when the phase jump between two consecutive elements jumps larger than π.

$$\psi(t) = \arctan \frac{B_Q(t)}{B_I(t)} + F \tag{3.21}$$

where:

$\psi(t)$ = Phase Variation
F = Phase Discontinuity

3.5 Vital Signs Estimation Algorithm: AMTC

3.5.1 Heart Rate

The phase signal from the Arctangent Demodulation algorithm can be used to estimate the heart rate of the subject [14]. As discussed in Section 3.4, the heart movement can be found in the phase signal. To extract the heart rate signal, a bandpass filter is applied. Since the human heart rate typically falls in the range of 40 and 150 bpm, the corresponding frequency range of *0.8 to 2.5 Hz* is used as the upper and lower limits of the filter, respectively. Many algorithms can also be used for vital sign detection. One of the most common methods for heart rate detection is to use a Fast Fourier Transform (FFT). By applying a FFT on the filtered phase signal, the strongest frequency is found which will correspond to a heart rate value. While high accuracy can be obtained using this method, problems occur when dealing with the harmonics of the respiration rate. The second and third harmonics of the breathing rate can show up as a stronger peak than the heart rate, which would cause incorrect estimations. To avoid harmonic interference, the Adaptive Multi-Trace Carving (AMTC) algorithm is used [22].

The AMTC algorithm excels in estimating and tracking weak frequency components that are rooted in noisy environments. Several other algorithms have been used for frequency tracking. The Yet Another Algorithm for Pitch Tracking (**YAAPT**) algorithm uses peak picking to detect multiple fundamental frequency candidates, and uses dynamic programming to determine the best frequency track from the set of candidates [23]. While performing well in high SNR settings, the algorithm becomes less accurate as the SNR decreases.

Using the AMTC algorithm allows us to combat these problems as it is based on iterative dynamic programming and adaptive trace compensation [22]. To detect the strongest frequency trace, AMTC uses a single-frequency trace tracking algorithm. Once the trace is detected, a flipped-Gaussian shaped function is applied to compensate/eliminate the trace, and the algorithm then searches for the next strongest frequency trace [22]. For the case of heart rate estimation, the algorithm only needs to detect the strongest frequency trace once, as the process of beamforming should theoretically make the signal from the subject the strongest frequency component.

To track and estimate the frequency trace, a spectrogram is first computed of the filtered phase variation signal, with M bins along the frequency axis and N bins along the time axis [22]. Next, an accumulated regularized maximum energy map, $G(m, n)$, is recursively computed using the spectrogram and the frequency transition probability matrix. The energy map, with size MxN, is calculated using Equation 3.22.

$$G(m,n) = \begin{cases} \mathbf{Z}(m,n) + \lambda \log P_m, & n = 1 \\ \\ \max\limits_{m'} \mathbf{G}(m', n-1) + \lambda \log P_{m'm} + \mathbf{Z}(m,n)\ , & n > 1 \end{cases} \tag{3.22}$$

where:

$\mathbf{G}(f(n), n)$ = Accumulated Regularized Maximum Energy Map

Z = Signal Spectrogram

P = Transition Probabiltiy Matrix

λ = Trace Smoothness Factor

Once $G(m, n)$ is computed, the maximum value in the last column of the map is denoted as $\hat{f}(n)(N)$, which represents the strongest frequency at time N. Next, the most optimal frequency trace solution is determined by backtracking from $\hat{f}(n)(N)$ to the beginning of the energy map[22]. This process can be expressed using Equation 3.23.

$$\hat{f}(n) = \underset{\hat{f}(n)}{\operatorname{argmax}} \mathbf{G}(f(n), n) + \lambda P_{f(n)\hat{f}(n+1)} \tag{3.23}$$

where:

$\hat{f}(n)$ = Estimated Frequency Trace

$\mathbf{G}(f(n), n)$ = Accumulated Regularized Maximum Energy Map

λ = Trace Smoothness Factor

P = Transition Probability Matrix

The following uniform walk transitions are considered: $P_{m\prime m} = \frac{1}{2k+1}, |m' - m| \leq k$, and $P_{m\prime m} = 0$. There are used in order to limit any frequency jumps of more than k frequency bins. This is beneficial for the case of heart rate estimation as the human heart is unable to make large jumps in frequency in a short period of time.

3.5.2 Respiration Rate

The AMTC method can also be used to find the estimated respiration rate values. As the normal respiration rate falls into the range of 6 to 48 BPM, a bandpass filter is applied to the phase variation signal with the corresponding frequency limits: *0.1 to 0.8 Hz*. This signal is then used as the input to the AMTC algorithm to determine the estimated breathing rate signal.

3.6 Conclusion

The signal processing chain for this work has been presented. Each part is presented in detail and their importance in vital signs is shown. Direction of arrival algorithms are introduced and compared, with the MUSIC algorithm being chosen for this work. The importance of beamforming is shown for cases involving multiple subjects. Lastly, the frequency tracing algorithm, AMTC, is explained, showing how to estimate both the heart rate and respiration rate of the subjects.

Chapter 4

Experiments/Results

To validate our algorithms and radar operation, we ran a series set of experiments with/without walls. Given that we are operating at mm-wave frequencies, only dry wall was utilized in these experiments. Meanwhile, single and multiple subject experiments were conducted. The following seven different experimental scenarios are performed:

1. Single Subject at Different Distances
2. Single Subject Through Drywall
3. Single Subject with Varying Angle
4. Multiple Subjects at Different Distances
5. Multiple Subjects Through Drywall
6. Multiple Subject at Varying Longitudinal Distance
7. Multiple Subject at Varying Lateral Distance

The first three experiments involve a single subject located in front of the radar. The last four experiments deal with cases involving multiple subjects. In all these experiments, the effect of distance and the impact of drywall are observed.

Each experiment was performed for 2 minutes. For a ground truth, the CONTEC CMS50D+ Contact Pulse Oximeter and the NUL-236 Respiration Monitor Belt Sensor were used to record the heart rate and respiration rates of the subject(s), respectively. The raw waveform was taken from the pulse oximeter and the respiration belt and processed to find the heart and respiration rate values. A sliding window of 15-seconds, with a 1 second step size, was applied on both the filtered radar heart and respiration rate signals to find their respected estimation signals. Similarly, the same sliding window is utilized on the raw waveform from the pulse oximeter and the respiration belt to find the ground truth heart rate and respiration rate. To quantify the accuracy for both heart rate and respiration rate results, the Mean Absolute Error (**MAE**) metric is used.

The configuration of the V-MD3 radar can be seen in Table 4.1, which corresponds to Radar Setting #9 from Table 2.2. Through various testing, this radar setting was chosen as it allows for the finest range resolution along with the use of all 8 Azimuth Channels. These additional channels allow for the angular resolution to be enhanced from 28.6° to 14.3°.

4.1 Single Subject Experiments

4.1.1 Single Subject at 1 Meter and 4 Meters

For the first experiment, a single subject was placed in front of the radar, aligned directly with the radar boresight. The setup can be seen in Figure 4.1. Two scenarios were performed with the subject first located 1 meter away from the radar and then moved to 4 meters away.

The direction of arrival estimation for the subject at 1 meter can be seen in Figure 4.2. From this map, we can see that the subject is located directly in front of the radar, i.e. broadside, at an estimated angle 0°. Figure 4.3 shows the results of the heart rate estimation. Here the AMTC algorithm shows high estimation accuracy as the Mean-Absolute Error of the heart rate came out to be 1.57 bpm. The respiration estimation for this case can be seen in Figure 4.4.

Table 4.1: Radar Configuration

Specs	VMD-3
Carrier Frequency	60 GHz
Sweep Bandwidth	3 GHz
Sampling Rate	4 MHz
Samples/Chirp	256
Sweep Slope	46875 kHz/μs
Chirps/Frame	5
Frame Rate	100 Hz
Range Resolution	0.05 m
Maximum Range	12.8 m

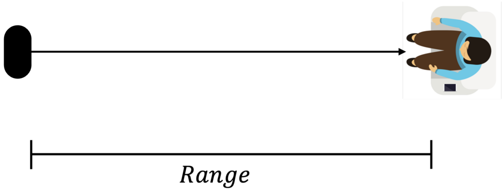

Figure 4.1: Setup for Single Subject Experiments

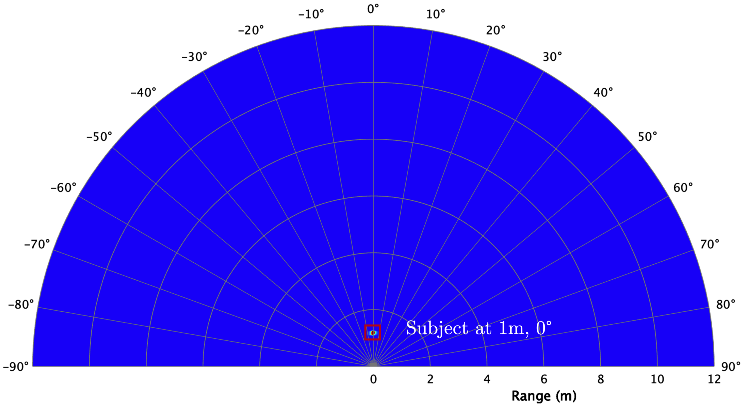

Figure 4.2: Direction of Arrival Map

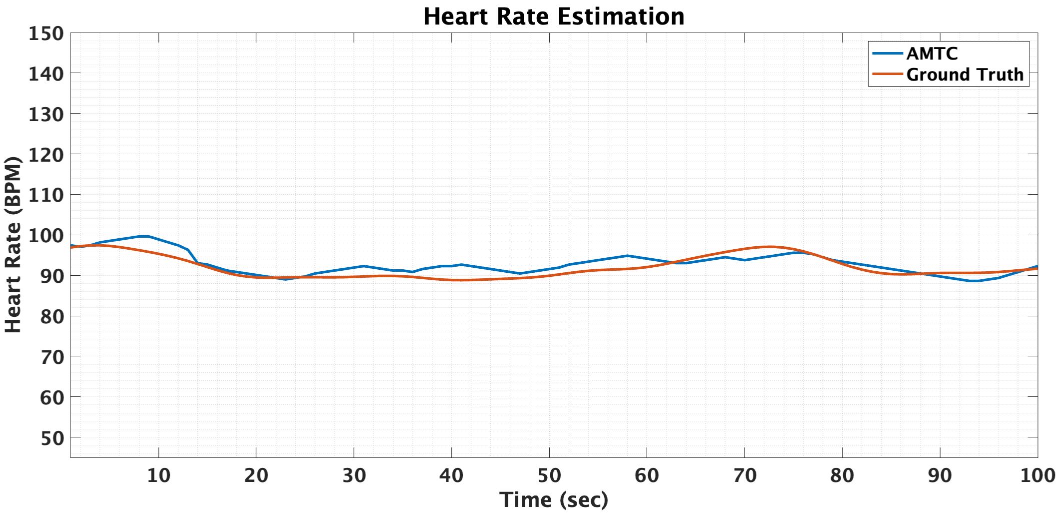

Figure 4.3: Heart Rate Results of Single Subject at 1 meter

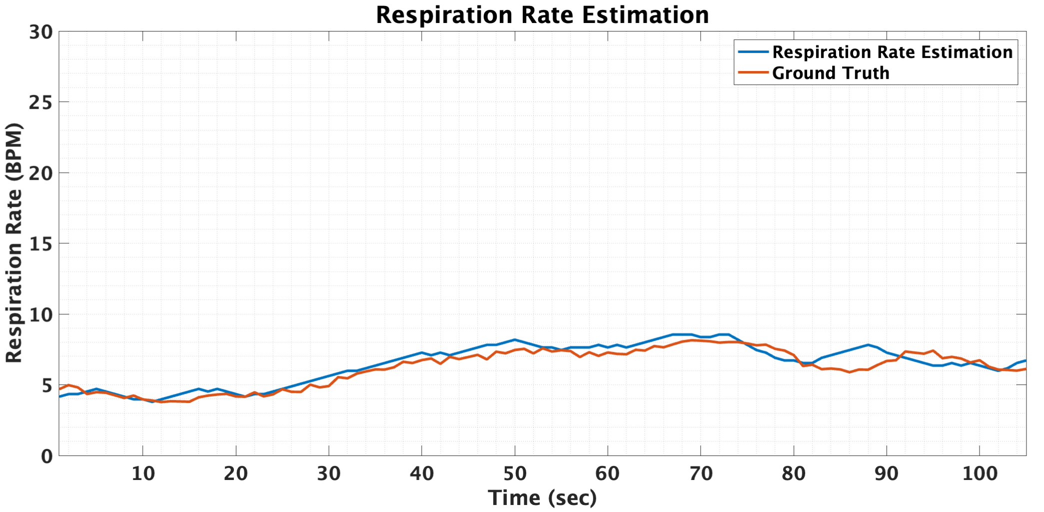

Figure 4.4: Respiration Rate Results of Single Subject at 1 meter

The experiments were then repeated with the subject moved back to 4 meters. The results for the vital sign estimations for both single subject cases are shown in Table 4.2. While the error in heart rate estimation increases as the distance increases from 1 to 4 meters, < 3 bpm error is still maintained. The respiration rate estimate for both cases obtained is < 0.5 bpm

4.1.2 Single Subject Through Drywall

In the second experiment, different thicknesses of drywall was placed 0.5 meters in front of the radar. Figure 4.5 shows the experiment setup. Using this setup, four different scenarios were performed, each with a different drywall:$\frac{1}{4}''$, $\frac{1}{2}''$, $\frac{5}{8}''$, and $1\frac{2}{8}''$. The subject was sitting in front of the radar at a range of 4 meters.

The $\frac{1}{4}''$ drywall scenario results can be found below. Figure 4.6 shows the direction of arrival map. From this map, the subject can be seen located at 4 meters and at an angle of $9°$, which is due to the effect of the drywall. The heart rate estimation result for this case can found in Figure 4.7. With a MAE of 2.31 bpm, the AMTC algorithm was able to maintain a similar accuracy to that of the no wall scenario shown in 4.2. Figure 4.8 shows the respiration rate estimate where a low error of 0.46 bpm is obtained.

The results for all the single subject drywall experiments can be seen in Table 4.3. Here we can see the error in the heart rate estimation increased as the thickness of the wall increases. While this is the case, we were able to obtain a less than 3 bpm error for each scenario. Low respiration rate errors were achieved for each case, as the error in breathing rate ranged from $0.31 - 0.46$ bpm.

Table 4.2: Single Subject Heart Rate and Respiration Rate Results

Distance	Heart Rate Error	Respiration Rate Error
1m	1.57 bpm	0.38 bpm
4m	2.13 bpm	0.46 bpm

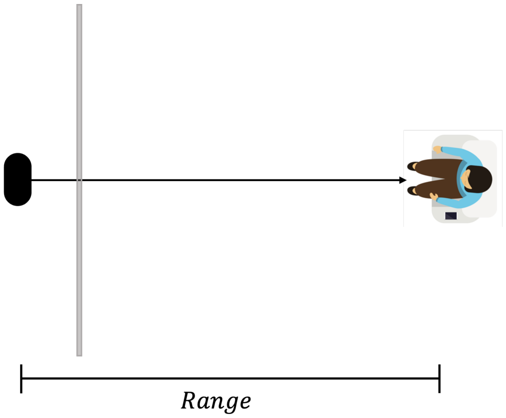

Figure 4.5: Setup for Through Wall Single Subject Experiments

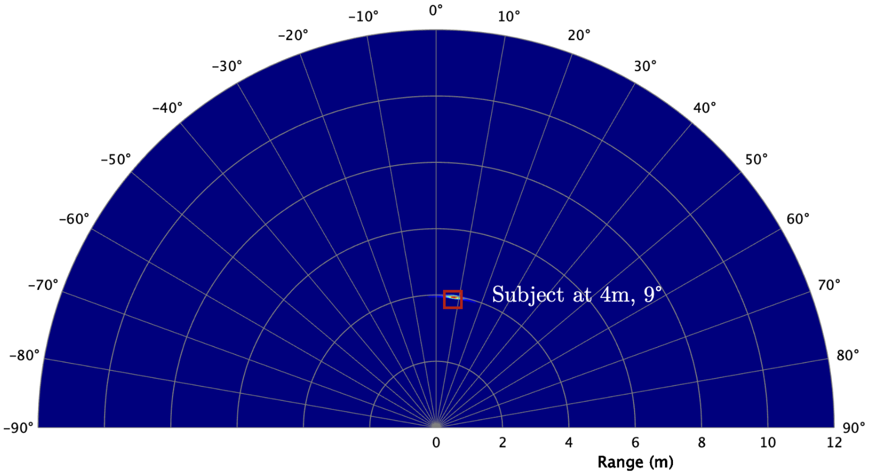

Figure 4.6: Direction of Arrival Map

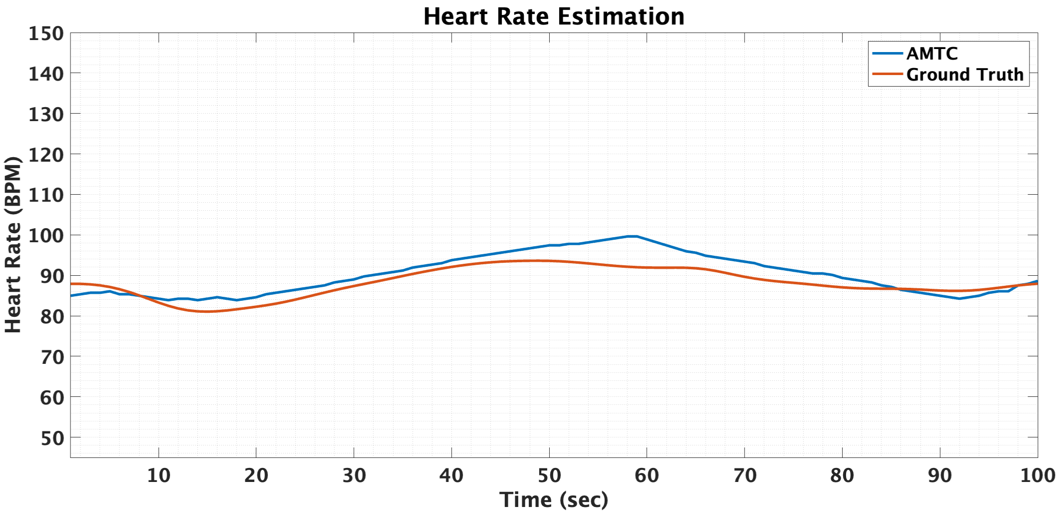

Figure 4.7: Heart Rate Results with $\frac{1}{4}''$ Drywall

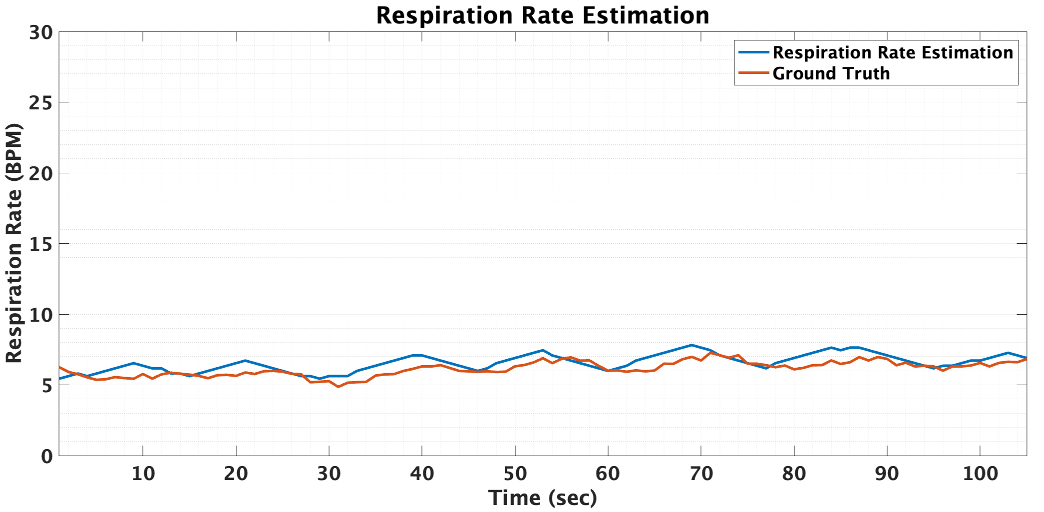

Figure 4.8: Respiration Rate Results with $\frac{1}{4}''$ Drywall

Table 4.3: Single Subject Through Wall Heart Rate and Respiration Rate Results

Distance	Drywall Thickness	Heart Rate Error	Respiration Rate Error
4m	1/4”	2.31 bpm	0.46 bpm
4m	1/2”	2.44 bpm	0.31 bpm
4m	5/8”	2.76 bpm	0.44 bpm
4m	1 1/4”	2.82 bpm	0.45 bpm

4.1.3 Single Subject at Varying Angle

In this experiment, the effect of angular location of the subject is observed. The setup, which can be seen in Figure 4.9, involves a single subject that is placed at fixed distance of 2 meters from the radar. Five scenarios were performed, with the subject being placed at the following angles to the left of the radars boresight: 0°, 20°, 40°, 60°, 80°.

The results for these cases can be seen in Table 4.4. When the subject is located at 0°, a high heart rate estimation is achieved as the mean absolute error is 1.58 bpm. Less than 2 bpm error was achieved as the subject is moved to 20° and 40°. However, the error starts to rapidly increase as the subject is moved to larger angles. When the subject is moved to 80°, the error in heart rate estimation becomes 2.76 bpm. From these results, we are able to see the error in heart rate increases as the angle θ_1 increases.

4.2 Multiple Subjects

4.2.1 Multiple Subjects at 1 Meter and 4 Meters

The fourth experiment performed involved two subjects located in front of the radar. Both subjects are located at the same range, with each located to the left and the right of the radars boresight. Figure 4.10 shows the setup. Similar to the single subject scenarios, the experiment is performed twice, once with the subjects at 1 meter from the radar and then repeated at a distance of 4 meters.

The following results involve the 1 meter scenario. The subject localization estimate can be seen in Figure 4.11, which places the subjects at 1 meter, with subject one located 15° to the left of the radar and subject 2 at 18° to the right of the radar. The heart rate estimation results can be found in Figure 4.12. From this figure, it can be seen that the both estimations were able to maintain high accuracy, as the error for both subjects were < 3 bpm.. Figure

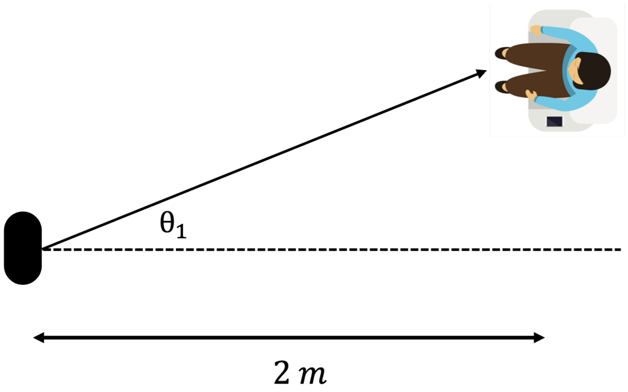

Figure 4.9: Setup for Single Subject with Varying Angle

Table 4.4: Single Subject with Varying Angle Results

Distance	Angle θ_1	Subject 1 Heart Rate Error
2m	0°	1.58 bpm
2m	20°	1.61 bpm
2m	40°	1.98 bpm
2m	60°	2.33 bpm
2m	80°	2.76 bpm

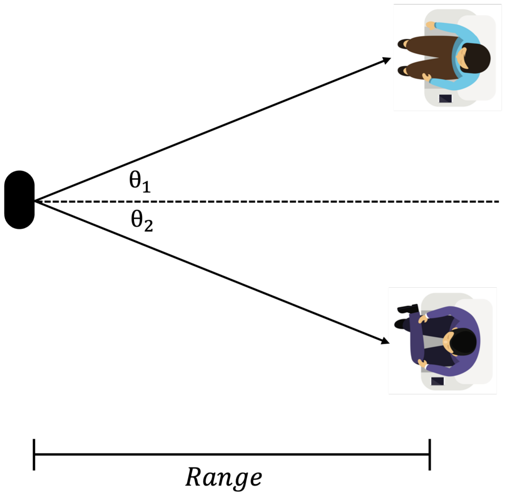

Figure 4.10: Setup for Multiple Subject Experiments

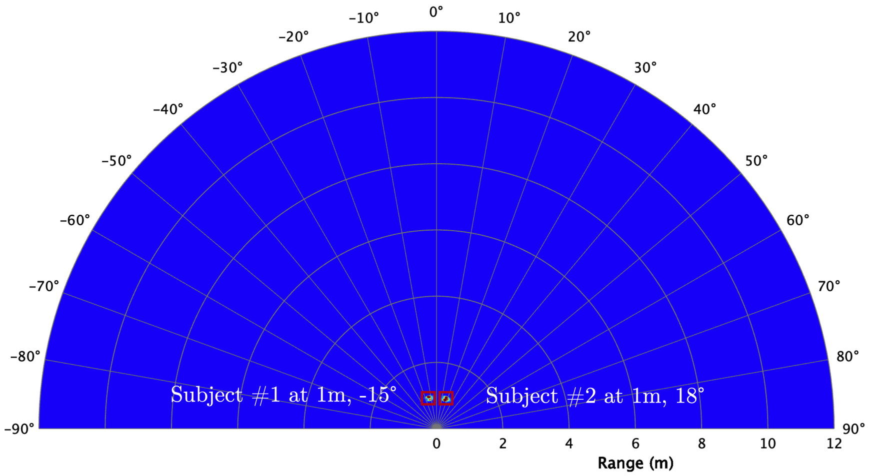

Figure 4.11: Direction of Arrival Map

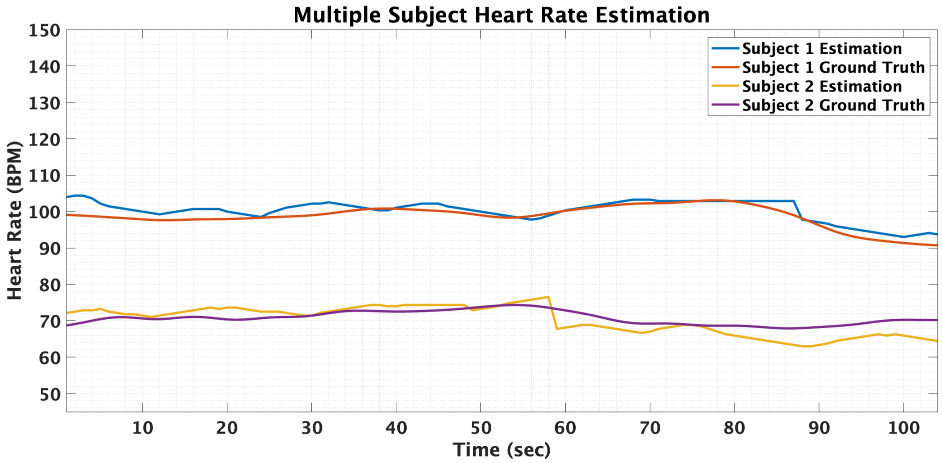

Figure 4.12: Heart Rate Results of Multiple Subjects at 1 meter

4.13 shows the respiration rate, where the error for Subject 1 and Subject 2 came out to be 0.36 bpm and 0.38 bpm, respectively.

The next case involved both subjects moving to a 4 meter distance from the radar. Table 4.6 shows the vital sign results for this scenario, as well as the 1 meter case. Similar to Experiment 1, the error in heart rate estimation for the 4 meter case was higher than the 1 meter case. While this is true, both estimation errors are < 3 bpm. Looking at the respiration rate for both cases, the error in each scenario was less than 0.5 bpm.

4.2.2 Multiple Subjects Through Drywall

The fifth experiment performed involved the addition of a drywall to the scene. Similar to the second experiment, different thicknesses of drywall were placed 0.5 meters in front of the radar. Four cases were tested, using the same drywall thicknesses as before, $\frac{1}{4}''$, $\frac{1}{2}''$, $\frac{5}{8}''$, and $1\frac{2}{8}''$. The setup for this experiment can be seen in Figure 4.14. Two subjects were again placed at the same range, with each located to the left and the right of the radars boresight.

Figure 4.15 shows the direction of arrival map, where subject one is located 15° to the left of the radar and subject 2 is at 18° to the right of the radar. Both of the subject are also seen to be at a 4 meter distance from the radar. Figure 4.16 displays the heart rate estimations for both subjects. The MAE for Subject 1 and Subject 2 came out to 2.14 bpm and 2.44 bpm, respectively. The respiration rate results are shown in Figure 4.17, where a low estimation error was obtained, with Subject 1 and Subject 2 having a 0.45 bpm and 0.49 bpm error, respectively.

The results for the remaining cases are displayed in Table 4.6. For each scenario, a low heart rate error was obtained, as both of the subjects had a < 3 bpm error. Similarly, high

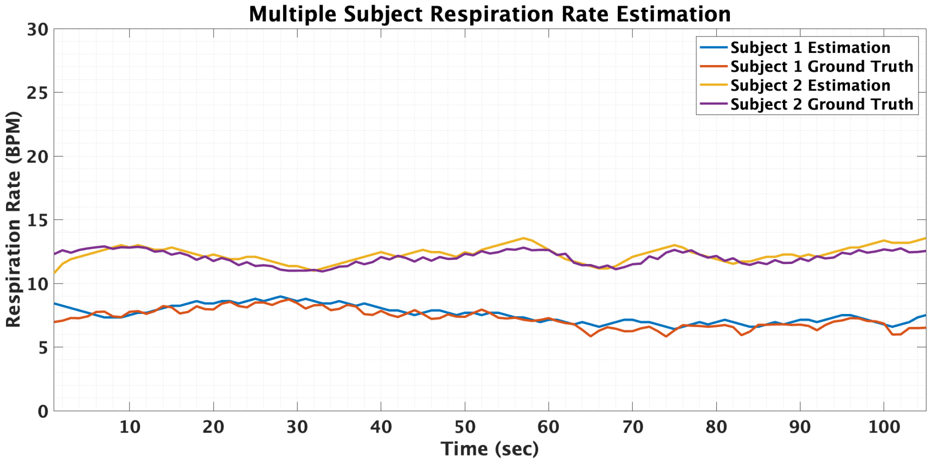

Figure 4.13: Respiration Rate Results of Multiple Subject at 1 meter

Table 4.5: Multiple Subject Heart Rate and Respiration Rate Results

Distance	Subject 1 Heart Rate Error	Subject 2 Heart Rate Error	Subject 1 Respiration Rate Error	Subject 2 Respiration Rate Error
1m	2.01 bpm	2.41 bpm	0.37 bpm	0.28 bpm
4m	2.28 bpm	2.49 bpm	0.43 bpm	0.33 bpm

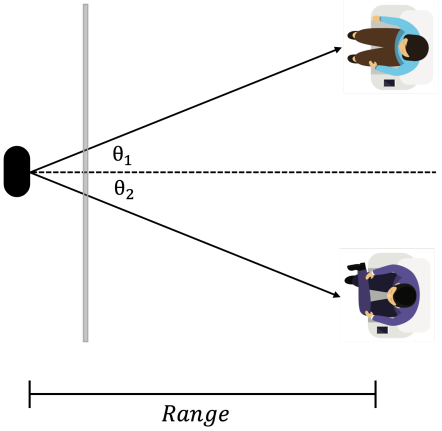

Figure 4.14: Setup for Through Wall Multiple Subject Experiments

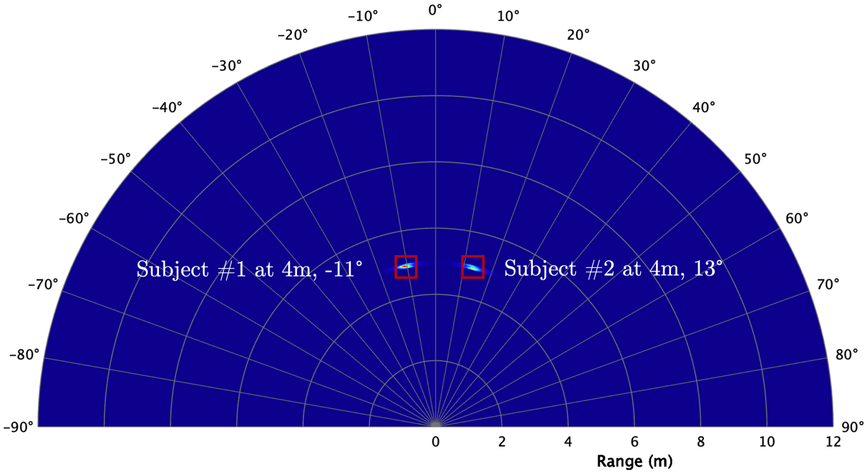

Figure 4.15: Direction of Arrival Map

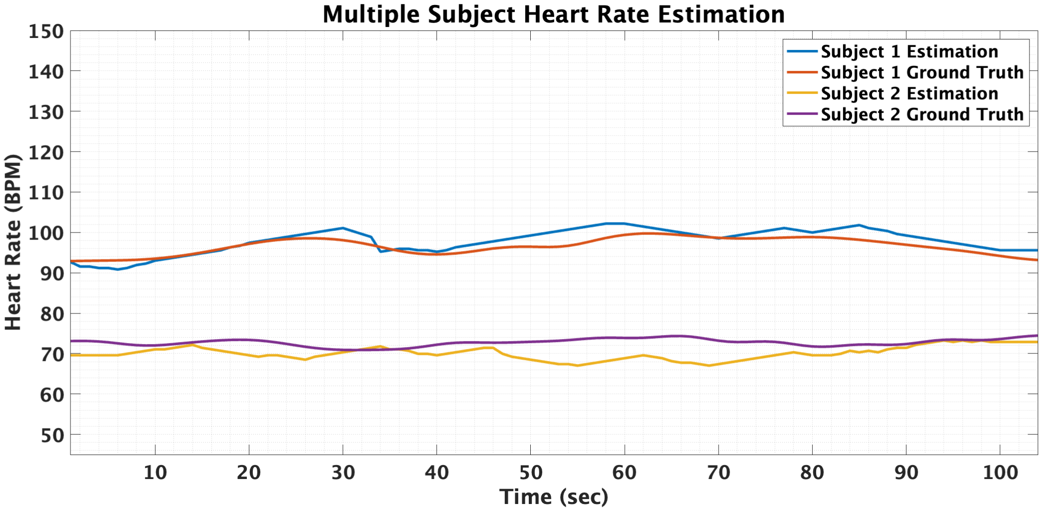

Figure 4.16: Heart Rate Results with $\frac{1}{4}''$ Drywall

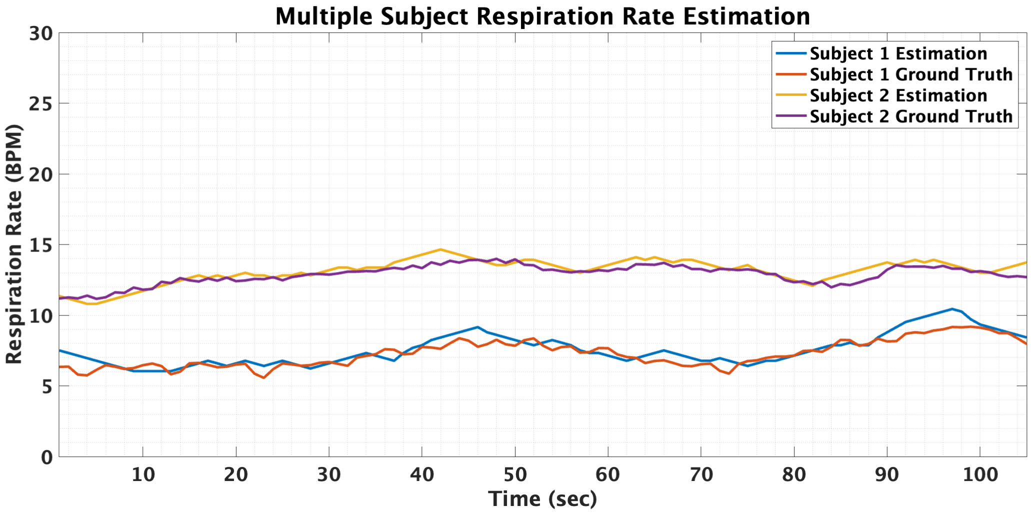

Figure 4.17: Respiration Rate Results with $\frac{1}{4}''$ Drywall

Table 4.6: Multiple Subject Through Wall Heart Rate and Respiration Rate Results

Distance	Drywall Thickness	Subject 1 HR Error	Subject 2 HR Error	Subject 1 RR Error	Subject 2 RR Error
4m	1/4”	2.14 bpm	2.44 bpm	0.45 bpm	0.49 bpm
4m	1/2”	2.57 bpm	2.49 bpm	0.36 bpm	0.38 bpm
4m	5/8”	2.41 bpm	2.87 bpm	0.33 bpm	0.43 bpm
4m	1 1/2”	2.37 bpm	2.96 bpm	0.43 bpm	0.45 bpm

accuracy was attained for the respiration rate, as for each scenario, both Subject 1 and 2 had a < 0.5 bpm error.

4.2.3 Multiple Subject at Varying Longitudinal Distance

In the sixth experiment, the effect of longitudinal spacing between multiple subjects is observed. Subject 1 is placed 1 meter away from the radar and the second subject is placed at four varying distances, defined as D_x: 1m, 2m, 3m and 4m. The lateral distance between the two subjects was fixed at 1 meter. The setup for this experiment can be seen in Figure 4.18. When D_x is set to 4 meters, high accuracy results were attained. However, as Subject 2 gets closer to Subject 1, the accuracy in heart rate estimation decreases. Table 4.7 displays the increase in heart rate as D_x decreases.

4.2.4 Multiple Subject at Varying Lateral Distance

The last experiment performed focused on the lateral distance between two subjects. Both subjects were located at a distance of 2 meters and the lateral distance, D_y, between them was varied. Figure 4.19 shows the setup for this experiment. Three cases were performed, with D_y set to the following distances: 1m, 1.25m, 1.5m. The results for this experiment can be found in Table 4.8. When the distance D_y increases from 1 meter to 1.5 meters, the heart rate estimations for both subjects also increases. This was expected because as the distance between the two subjects increase, the vital sign signals of both subjects can clearly be separated from each other, which allow for accurate results.

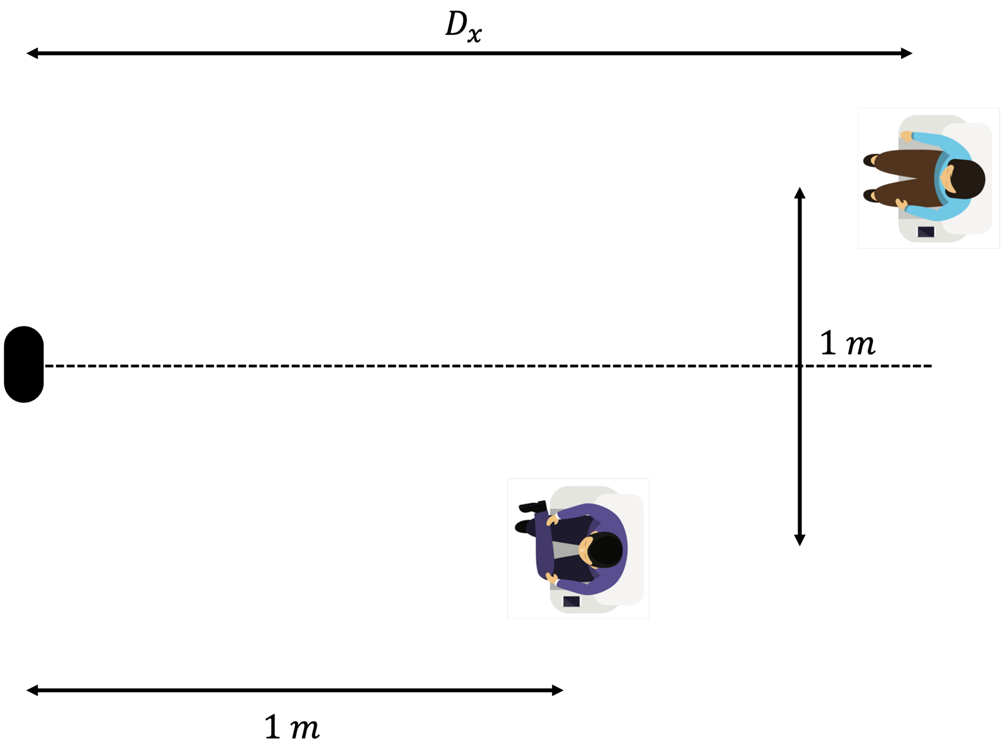

Figure 4.18: Setup for Multiple Subject at Varying Longitudinal Distance

Table 4.7: Multiple Subject at Varying Longitudinal Distance Results

Subject 1 Distance	Subject 2 Distance: D_X	Subject 1 Heart Rate Error	Subject 2 Heart Rate Error
1m	4m	1.55 bpm	2.00 bpm
1m	3m	1.59 bpm	2.02 bpm
1m	2m	1.89 bpm	2.18 bpm
1m	1m	2.11 bpm	2.45 bpm

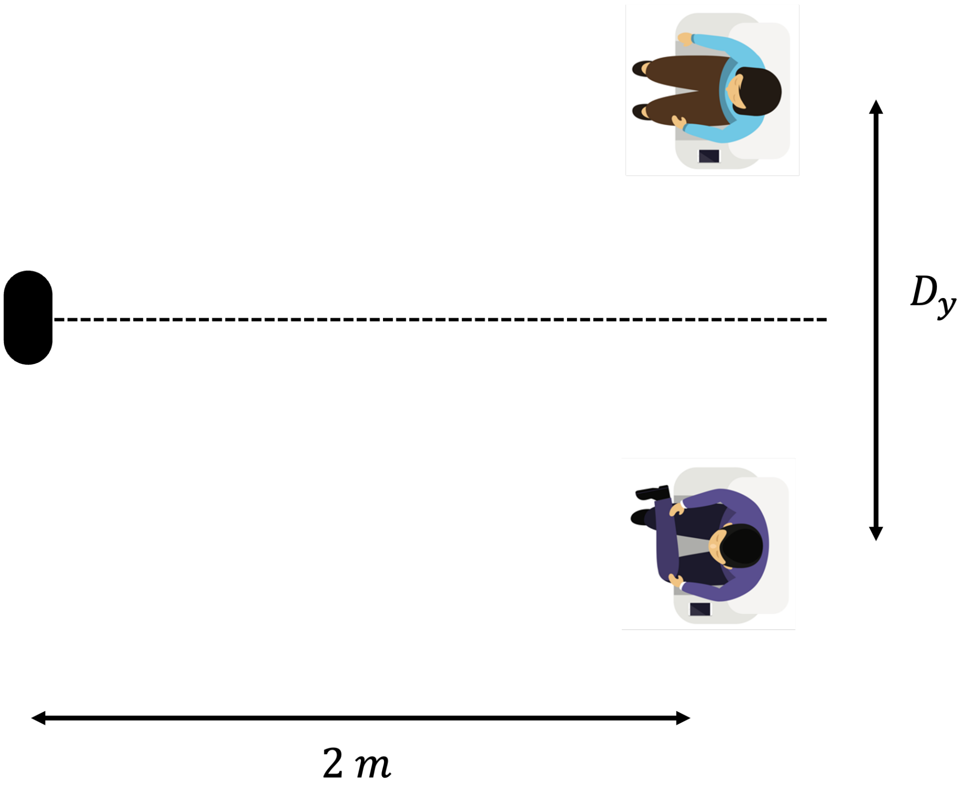

Figure 4.19: Setup for Multiple Subject at Varying Lateral Distance

Table 4.8: Multiple Subject at Varying Lateral Distance Results

Subject 1 and 2 Distance	Lateral Distance: D_y	Subject 1 Heart Rate Error	Subject 2 Heart Rate Error
2m	1.5m	2.01 bpm	2.48 bpm
2m	1.25m	2.09 bpm	2.65 bpm
2m	1m	2.17 bpm	2.75 bpm

4.3 Results Comparison

To validate our results, the following two comparison tables are shown of each experiment against similar state of the art work. Table 4.9 compares the single subject results obtained with other reported research while Table 4.10 is comparing the scenarios of multiple subjects at against other works. Prior works include radars working at both low frequencies, as well as systems operating in the mmWave frequency range. As can be seen in Tables 4.9 - 4.10, the detection error obtained for both the heart rate and respiration rate estimations in this work are comparable with the prior works.

4.4 Conclusion

In this work, a commercial radar is utilized for vital sign detection. Operating at 60 GHz with a bandwidth of 3 GHz, this radar has MIMO antenna configuration of 3 Transmitting Antennas and 4 Receiving Antennas. Using this radar, an algorithm was designed to estimate the vital signs of humans. Using direction of arrival, beamforming and the Adaptive Multi-Trace Carving (AMTC) algorithm, we can clearly estimate vital signs of humans with an error < 3 bpm for heart rate and < 1 bpm for respiration rate. The accuracy is maintained even with the presence of drywall, with a thickness up to 1 1/4".

Table 4.9: Comparison of Single Subject Work With Alternative State-Of-The-Art Research

Work	Signal Processing	Operating Frequency	Through Wall	Distance	RR Error	HR Error
This Work	AMTC	60 GHz	No	1m	0.38 bpm	1.57 bpm
This Work	AMTC	60 GHz	No	4m	0.46 bpm	2.13 bpm
This Work	AMTC	60 GHz	Yes	4m	0.45 bpm	2.82 bpm
Sacco et al.[10]	FFT	5.8 GHz	No	1.5m	< 1 bpm	< 2 bpm
Yang et al.[11]	FFT	60 GHz	No	2m	0.43 bpm	2.15 bpm
Wang et al.[24]	Dynamic Programming	60 GHz	No	1m	0.14 bpm	1.29 bpm
M. Mercuri et al.[9]	Wavelet Decomposition	7.3-8.3 GHz	No	4m	0.24 bpm	1.43 bpm
Rong[6]	Adaptive 2^{nd} Harmonic Selection	7.3 GHz	Yes	1.5m	-	< 2 bpm
Wang et al.[24]	Dynamic Programming	60GHz	Yes	1m	0.29 bpm	5.25 bpm
Al-Wahedi et al.[25]	FFT	8 GHz	Yes	0.7m	1.92 bpm	5.54 bpm

Table 4.10: Comparison of Multiple Subjects Work With Alternative State-Of-The-Art Research

Work	Signal Processing	Operating Frequency	Through Wall	Distance	RR Error	HR Error
This Work	AMTC	60 GHz	No	(1m, 1m)	0.33 bpm	2.21 bpm
This Work	AMTC	60 GHz	No	(4m, 4m)	0.38 bpm	2.39 bpm
This Work	AMTC	60 GHz	Yes	(4m, 4m)	0.44 bpm	2.67 bpm
M. Mercuri et al.[9]	Wavelet Decomposition	7.3-8.3 GHz	No	(4m, 4m)	0.39 bpm	1.39 bpm
Li et al.[5]	VMD	1.75 - 2.25 GHz	No	(2.5m, 2.5m)	0.84 bpm	2.63 bpm
F. Wang et al.[26]	Custom FEA	5.8 GHz	No	(2.5m, 1.9m)	< 2 bpm	< 3 bpm
Rong[6]	Adaptive 2^{nd} Harmonic Selection	7.3 GHz	Yes	(2m, 1m)	-	< 2 bpm
Yang et al.[11]	FFT	60 GHz	Yes	-	0.58 bpm	-

Chapter 5

Conclusion

The use of radars is becoming more and more popular for biomedical applications. Various types of radar have been used for vital sign detection including CW, Pulse, and FMCW radars. In recent years, FMCW radars are being used more often due to their high range resolution and wide bandwidth. With the development of millimeter wave radars and integrating the antennas on the same package, chips are becoming smaller and smaller, which allows for a compact radar. While previous vital sign detection has been done using lower frequency radars in order to minimize cost and maximize performance, prior work has shown the ability to use higher frequency radars for these same tasks. In this work, the ability to use portable radars for vital sign applications has been shown. This work has also shown the ability to accurately detect vitals signs of up to two subjects with the use of a millimeter-wave radar, but could be extended to multiple subjects.

5.1 Summary of Results

The signal processing chain showed in this work has allowed for accuracies of heart rate estimation below 3 bpm error and respiration rates even lower at 1 bpm error. The ability for MIMO antenna configuration allowed for direction of arrival techniques and channel combining, which allowed for improvements in SNR. With the combination of direction of arrival, beamforming, and the AMTC algorithm for heart rate and respiration rate detection, results comparable to lower frequency radars were obtained.

Multiple experiments were performed in this work to determine different scenarios that are viable. Single subject experiments were performed at distances of 1 meter and 4 meters. Through wall scenarios were also conducted with varying thicknesses of drywall, in order to see radar operation limits. These two experiments were then repeated with multiple subjects at the same range. All these experiments were compared to state of the art results from both lower and higher frequency radar systems. The accuracies obtained in the experiments were comparable to those of larger, lower frequency radars. From these experiments, I was able to see the effects that the subjects distance from the radar has on heart rate estimation. As the distance increases, the heart rate error also increases. Even with the increase in error, I was able to attain heart accuracies below 3 bpm. The final single subject experiment performed involved varying the angle of the subject from the radar. As the angle increased from 0° to 80°, the accuracy in heart rate estimation decreased. When performing the multiple subject experiments, we were also able to see the effect of lateral and longitudinal distance between the two subjects. As the lateral distance between the two subjects increased, the accuracy of heart rate estimation decreased. However, as the distance between them increased, the vital signs accuracy also increased. This was expected since the farther the subjects are, the bigger the separation of the vital sign signals from each subject, which allows for clean extractions of both signals. While the non line of sight experiments typically had higher errors than line of sight scenarios, we were still able to achieve < 3 bpm error in heart rate estimation and < 1 bpm error in breathing rate.

5.2 Future Work

The next steps of this work include the testing of vital sign detection of moving subjects. While many tasks involve a sitting or lying subject, the ability to measure vitals signs of a moving subjects open a new field of applications. The biggest step is to move away from using a laptop/computer and use a single board computer. Devices such as the UDOO Bolt and the NVIDIA Jetson Xavier NX allow for supercomputer performance from a small, portable device. Replacing the computer with these devices allow for the entire system to decrease in size, which will allow for a more portable system.

Bibliography

[1] Artit Rittiplang and Pattarapong Phasukkit. 1-tx/5-rx through-wall uwb switched-antenna-array radar for detecting stationary humans. *Sensors*, 20(23), 2020. ISSN 1424-8220. doi: 10.3390/s20236828. URL `https://www.mdpi.com/1424-8220/20/23/6828`. 3

[2] Zhipeng Hu, Zhaofa Zeng, Kun Wang, Weike Feng, Jianmin Zhang, Qi Lu, and Xiaoqian Kang. Design and analysis of a uwb mimo radar system with miniaturized vivaldi antenna for through-wall imaging. *Remote Sensing*, 11(16), 2019. ISSN 2072-4292. doi: 10.3390/rs11161867. URL `https://www.mdpi.com/2072-4292/11/16/1867`. 3

[3] Constantine Balanis. *Antenna theory: Analysis and design*. Wiley-Interscience, 2016. 5

[4] URL `https://www.ti.com/lit/pdf/spry334`. 7

[5] Zhi Li, Tian Jin, Yongpeng Dai, and Yongkun Song. Through-wall multi-subject localization and vital signs monitoring using uwb mimo imaging radar. *Remote Sensing*, 13(15), 2021. ISSN 2072-4292. doi: 10.3390/rs13152905. URL `https://www.mdpi.com/2072-4292/13/15/2905`. 7, 8, 76

[6] Yu Rong. *Remote Sensing For Vital Signs Monitoring Using Advanced Radar Signal Processing Techniques*. PhD thesis, Arizona State University, January 2018. 7, 8, 75, 76

[7] Khadija Hanifi and M. Elif Karsligil. Elderly fall detection with vital signs monitoring using cw doppler radar. *IEEE SENSORS JOURNAL*, 21(15):16969–16978, AUG 1 2021. ISSN 1530-437X. doi: 10.1109/JSEN.2021.3079835. 7, 8

[8] Marco Mercuri, Yao-Hong Liu, Ilde Lorato, Tom Torfs, Fokko Wieringa, André Bourdoux, and Chris Van Hoof. A direct phase-tracking doppler radar using wavelet independent component analysis for non-contact respiratory and heart rate monitoring. *IEEE Transactions on Biomedical Circuits and Systems*, 12(3):632–643, 2018. doi: 10.1109/TBCAS.2018.2813013. 7, 8

[9] Marco Mercuri, Giulia Sacco, Rainer Hornung, Peng Zhang, Hubregt J. Visser, Martijn Hijdra, Yao-Hong Liu, Stefano Pisa, Barend van Liempd, and Tom Torfs. 2-d localization, angular separation and vital signs monitoring using a siso fmcw radar for smart long-term health monitoring environments. *IEEE Internet of Things Journal*, 8(14):11065–11077, 2021. doi: 10.1109/JIOT.2021.3051580. 8, 9, 75, 76

[10] Giulia Sacco, Emanuele Piuzzi, Erika Pittella, and Stefano Pisa. An fmcw radar for localization and vital signs measurement for different chest orientations. *Sensors*, 20 (12), 2020. ISSN 1424-8220. doi: 10.3390/s20123489. URL `https://www.mdpi.com/1424-8220/20/12/3489`. 8, 9, 75

[11] Zhicheng Yang, Parth H. Pathak, Yunze Zeng, Xixi Liran, and Prasant Mohapatra. Monitoring vital signs using millimeter wave. In *Proceedings of the 17th ACM International Symposium on Mobile Ad Hoc Networking and Computing*, MobiHoc '16, page 211–220, New York, NY, USA, 2016. Association for Computing Machinery. ISBN 9781450341844. doi: 10.1145/2942358.2942381. URL `https://doi.org/10.1145/2942358.2942381`. 8, 9, 75, 76

[12] Merrill I. Skolnik. *Radar Handbook*. McGraw-Hill, 2008. 13, 14, 19

[13] MARK A. RICHARDS. *Fundamentals of Radar Signal Processing.* MCGRAW-HILL EDUCATION, 2014. 14

[14] Yong Wang, Wen Wang, Mu Zhou, Aihu Ren, and Zengshan Tian. Remote monitoring of human vital signs based on 77-ghz mm-wave fmcw radar. *Sensors*, 20(10):2999, 2020. doi: 10.3390/s20102999. 14, 52

[15] P. P. Vaidyanathan and Piya Pal. Mimo radar, simo radar, and ifir radar: a comparison. In *2009 Conference Record of the Forty-Third Asilomar Conference on Signals, Systems and Computers*, pages 160–167, 2009. doi: 10.1109/ACSSC.2009.5470139. 22

[16] URL `https://www.ti.com/lit/an/swra554a/swra554a.pdf`. 23, 36

[17] URL `https://www.rfbeam.com/files/products/41/downloads/Datasheet_V-MD3.pdf`. 26

[18] Tarun Banka, Aditya Maroo, Anura Jayasumana, and V. Chandrasekar. Radar networking: Considerations for data transfer protocols and network characteristics. 01 2005. 26

[19] Zhizhang Chen, Gopal Gokeda, and Yiqiang Yu. *Introduction to direction-of-arrival estimation.* Artech House, 2010. 36, 38, 39, 42, 44

[20] B.D. Van Veen and K.M. Buckley. Beamforming: a versatile approach to spatial filtering. *IEEE ASSP Magazine*, 5(2):4–24, 1988. doi: 10.1109/53.665. 41, 48

[21] Constantine A. Balanis and Panayiotis I. Ioannides. *Introduction to smart antennas.* Morgan amp; Claypool, 2007. 42

[22] Qiang Zhu, Mingliang Chen, Chau-Wai Wong, and Min Wu. Adaptive multi-trace carving based on dynamic programming. In *2018 52nd Asilomar Conference on Signals,*

Systems, and Computers, pages 1716–1720, 2018. doi: 10.1109/ACSSC.2018.8645216. 53, 54

[23] Stephen Zahorian and Hongbing Hu. A spectral/temporal method for robust fundamental frequency tracking. *The Journal of the Acoustical Society of America*, 123:4559–71, 07 2008. doi: 10.1121/1.2916590. 53

[24] Fengyu Wang, Feng Zhang, Chenshu Wu, Beibei Wang, and K. J. Ray Liu. Vimo: Multiperson vital sign monitoring using commodity millimeter-wave radio. *IEEE Internet of Things Journal*, 8(3):1294–1307, 2021. doi: 10.1109/JIOT.2020.3004046. 75

[25] Ali Al-Wahedi, Mojtaba Al-Shams, Mohammed Aieash Albettar, Saleh Alawsh, and Ali Muqaibel. Wireless monitoring of respiration and heart rates using software-defined-radio. In *2019 16th International Multi-Conference on Systems, Signals Devices (SSD)*, pages 529–532, 2019. doi: 10.1109/SSD.2019.8893254. 75

[26] Fu-Kang Wang, Pin-Hsun Juan, De-Ming Chian, and Chao-Kai Wen. Multiple range and vital sign detection based on single-conversion self-injection-locked hybrid mode radar with a novel frequency estimation algorithm. *IEEE Transactions on Microwave Theory and Techniques*, 68(5):1908–1920, 2020. doi: 10.1109/TMTT.2020.2967372. 76

Vita

Marvin Joshi was born in Aberdeen, Maryland in 1998. He grew up in Vancouver, WA and has lived in Knoxville, TN since 2012. In 2016, he attended the University of Tennessee, Knoxville, in pursuit of his Bachelor's Degree in Electrical Engineering. He became a undergraduate teaching assistant in 2019 and later that year, he joined the Microwave Research Group. After receiving his Bachelor's degree in 2020, he then continued at the University of Tennessee, Knoxville as a graduate research and teaching assistant in pursuit of his Master's degree. His interests include circuit design, RF/Microwave engineering and digital signal processing.